JM PAPERS

Experimental investigation of aerofoil tonal noise at low Mach number

Prateek Jaiswal[1], Yann Pasco[1], Gyuzel Yakhina[1] and Stéphane Moreau[1],†

[1]Department of Mechanical Engineering, University of Sherbrooke, Sherbrooke, QC, J1K 2R1, Canada

This paper presents an experimental investigation of aerofoil tones emitted by a controlled-diffusion aerofoil at low Mach number (0.05), moderate Reynolds number based on the chord length (1.4×10^5) and moderate incidence ($5°$ angle of attack). Wall-pressure measurements have been performed along the suction side of the aerofoil to reveal the acoustic source mechanisms. In particular, a feedback loop is found to extend from the aerofoil trailing edge to the regions near the leading edge where the flow encounters a mean favourable pressure gradient, and consists of acoustic disturbances travelling upstream. Simultaneous wall-pressure, velocity and far-field acoustic measurements have been performed to identify the boundary-layer instability responsible for tonal noise generation. Causality correlation between far-field acoustic pressure and wall-normal velocity fluctuations has been performed, which reveals the presence of a Kelvin–Helmholtz-type modal shape within the velocity disturbance field. Tomographic particle image velocimetry measurements have been performed to understand the three-dimensional aspects of this flow instability. These measurements confirm the presence of large two-dimensional rollers that undergo three-dimensional breakdown just upstream of the trailing edge. Finally, modal decomposition of the flow has been carried out using proper orthogonal decomposition, which demonstrates that the normal modes are responsible for aerofoil tonal noise. The higher normal modes are found to undergo regular modulations in the spanwise direction. Based on the observed modal shape, an explanation of aerofoil tonal noise amplitude reduction is given, which has been previously reported in modular or serrated trailing-edge aerofoils.

Key words: aeroacoustics, boundary layer stability, turbulent transition

1. Introduction

The unmanned aerial vehicle (UAV) and small micro air vehicle (MAV) industries are expected to grow at a compound annual growth rate of approximately 20.7 % yearly until

† Email address for correspondence: stephane.smoreau@gmail.com

2022 (MRC Statistics 2016). Like UAVs and MAVs, micro-turbine and small scale cooling fans used in ventilation systems operate at low to moderate Reynolds numbers based on the tip chord and low tip Mach numbers. These lifting devices have become omnipresent in our society. Consequently, noise emitted by these devices and their impact on human health and comfort cannot be overlooked. Therefore, aerofoils operating in such Reynolds and Mach number regimes need to be optimised not only for lift and drag but also for noise. Among the various aerofoil self-noise mechanisms (see Brooks, Pope & Marcolini (1989), for classifications of aerofoil self noise), aerofoil tonal noise can in particular be a cause of major annoyance. This is because tonal noise is several dB higher than the corresponding broadband noise (see Nash, Lowson & McAlpine (1999), for instance). At low to moderate Reynolds numbers based on chord length Re_c (from 5×10^4 to 6×10^5) an aerofoil has been shown to generate an intense whistling sound. Paterson *et al.* (1973) and Fink (1975) were probably the first to show that aerofoil tonal noise was caused by a nonlinear feedback mechanism in which the tonal frequency locked in over certain flow speeds, and jumped to a different frequency when the flow speed was increased. The resulting ladder-type structure of tonal noise frequencies with flow speed was later confirmed by many studies on different aerofoils (Arbey & Bataille 1983; Kingan & Pearse 2009; Chong & Joseph 2012; Pröbsting, Scarano & Morris 2015; Padois *et al.* 2016; Yakhina *et al.* 2020) including the present controlled-diffusion (CD) aerofoil, as illustrated in figure 1(*a*). As shown by Padois *et al.* (2016), the frequency of the primary tone f_S on the CD aerofoil follows Paterson's law (Paterson *et al.* 1973), confirmed by Arbey & Bataille (1983) on several NACA 0012 and modified NACA 0012 (termed NACA 0012*) aerofoils

$$f_S = KU_\infty^{1.5}/\sqrt{C\nu}, \tag{1.1}$$

but with a constant $K(\simeq 0.017)$ larger than for the NACA 0012 cases ($\simeq 0.011$). Here, C is the chord length, U_∞ the free-stream velocity and ν is the fluid kinematic viscosity. The secondary tones f_n, evidence of a feedback loop, also follow a power law with velocity but with a shallower slope (Tam 1974). Moreover, Padois *et al.* (2016) have also confirmed the nonlinear origin of tonal noise with wavelet and bicoherence spectral analyses on the CD aerofoil, and have also shown that several tonal noise regimes exist, particularly a regime with a single and strongly intermittent tone, which is the targeted flow condition of the present study. As illustrated in figure 1(*b*), the present flow condition marked by a star lies at the junction between a single steady tone and multiple tones on this aerofoil, and closely corresponds to the critical limit for tonal noise on the NACA 0012 aerofoil, which makes the present case appealing for detailed aero-acoustic analysis.

Several authors (see Nash *et al.* (1999), Desquesnes, Terracol & Sagaut (2007), de Pando (2012), Pröbsting (2015) and Padois *et al.* (2016), for instance) have reported the presence of flow instability near the trailing edge, whenever aerofoil tones are heard. With a global stability analysis, de Pando (2012) argues that these boundary-layer instabilities are convectively unstable (Huerre & Monkewitz 1985), as such the existence of self-sustained tonal noise would require an existence of a feedback loop. Similarly, Wu, Sandberg & Moreau (2021) performed a global stability analysis on three different direct numerical simulation (DNS) databases at similar Reynolds and Mach numbers on two different aerofoils. They showed that the flow separation and reattachment at the trailing edge on the suction side of the aerofoil seems to be the only prerequisite of the establishment of the feedback loop, regardless of the presence of tones in the DNS. Several aerofoil tonal noise studies have previously evidenced the existence of a feedback loop (see Arcondoulis *et al.* (2013), Pröbsting (2015), Arcondoulis, Liu & Xu (2019) and Yakhina (2017), for instance). Tam & Reddy (1977) were the first to pitch the idea of a feedback
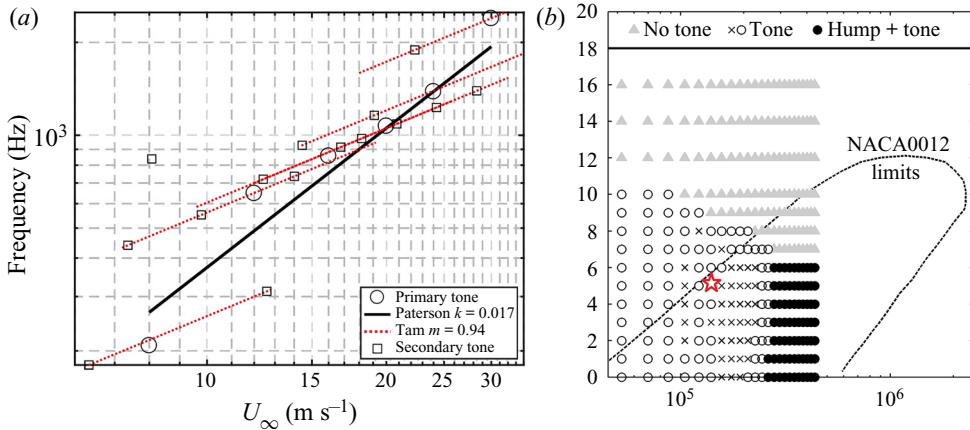
Figure 1. Tonal noise on the CD aerofoil: (*a*) evolution of the frequency of tones vs flow velocity, demonstrating the ladder-type structure (Paterson *et al.* 1973); (*b*) presence of tones as a function of Reynolds number and angle of attack (present case marked with a red star).

loop between acoustic sources in the wake and upstream boundary-layer disturbances. In contrast, Arbey & Bataille (1983) reasoned that the acoustic disturbance generated at the trailing edge instead is responsible for the feedback loop. Nash *et al.* (1999) conjectured that hydrodynamic instabilities present near the trailing edge or in the near wake were responsible for feedback. Nash *et al.* (1999) laid a hypothesis that large scale hydrodynamic oscillations are responsible for that frequency selection, which results in acoustic tones. Gelot & Kim (2020) gave indirect evidence of acoustic feedback using Arbey & Bataille's (?)emi-empirical formula. However, Gelot & Kim's (?)nalysis assumes constant convective velocity, which is in disagreement with their own results and previous measurement data (Yakhina *et al.* 2020). Furthermore, Gelot & Kim's (?)nalysis assumes that acoustic wave fronts enter the laminar separation bubble (LSB) region. This claim cannot be substantiated without a receptivity analysis. In particular, the LSB must be shown to convert the longer acoustic waves to shorter hydrodynamic waves or pressure gusts. This is especially true for low Mach number flows because the ratio of the acoustic to hydrodynamic wavelength is inversely proportional to the Mach number. In fact, for low Mach number flows, analytical results of leading-edge receptivity theory (Goldstein 1983; Saric, Reed & Kerschen 2002) point to the leading edge as the most probable location where wavelength conversion of the disturbances can take place. In addition, when an aerofoil is acoustically excited, Pröbsting & Yarusevych (2021) have demonstrated that the wavelength conversion processes take place in the leading-edge region of the aerofoil. Furthermore, Yakhina *et al.* (2020) have found the existence of principal and secondary tone frequencies in their wall-pressure spectra measurements. These high-amplitude peaks have also been measured by the probes that are located close to the leading edge of the aerofoil. Since the disturbance induced by the hydrodynamic events is likely to be damped more quickly than acoustic disturbances, which are known to propagate with little attenuation, these peaks in the wall-pressure spectra (measured at the leading edge of the aerofoil) are likely caused by acoustic disturbances. However, a more direct proof is lacking that would confirm the precise nature of the disturbances. Therefore, the first objective of this paper is to substantiate the existence of a feedback loop, and provide direct evidence as to whether this feedback loop is acoustic or hydrodynamic in nature. In order to show

the presence of principal and secondary tone peaks, the wall-pressure spectra close to the leading edge are measured in the case of the CD aerofoil. For the tonal noise generated by an aerofoil, this will help to identify the region of wavelength (acoustic to hydrodynamic) conversion.

Acoustic or hydrodynamic forcing has important consequences for the flow transition and boundary-layer instability. In particular, it has been shown that Kelvin–Helmholtz-type instabilities are receptive to disturbances generated by an external acoustic source (Andan & Lee 2018; Kurelek, Kotsonis & Yarusevych 2018; Kurelek, Yarusevych & Kotsonis 2019; Pröbsting & Yarusevych 2021) or a plasma actuator (Michelis, Yarusevych & Kotsonis 2018*b*). The type of boundary-layer instability that generates aerofoil tones has been a source of controversy in the past. Tam & Reddy (1977), for example, had conjectured a Tollmien–Schlichting (TS) flow instability to be responsible for the emission of aerofoil tones. The TS waves are the first stages of flow transition from the laminar to the turbulent boundary layer. However, Atassi (1984) pointed out that the flow separation near the trailing edge implies the presence of separated shear flow-type instability, similar to that of Kelvin–Helmholtz type. This has been supported more recently by de Pando (2012) and Pröbsting & Yarusevych (2015). In particular, Pröbsting & Yarusevych (2015) argued that the velocity fluctuations measured near the trailing edge exceed the fluctuations typically present in TS wave instability. Recently, Sanjose *et al.* (2019) performed a three-dimensional DNS on the CD aerofoil in the present flow regime, and found a Kelvin–Helmholtz-type instability to be the cause of tonal noise. Therefore, the second objective of the present study is to experimentally confirm the findings of Sanjose *et al.* (2019).

Once the nature of the boundary-layer instability responsible for aerofoil tones has been established, it will be helpful to understand the modal structure of the boundary-layer instability from a noise or flow-control point of view. Previous experimental investigations confirm the presence of a LSB (Nash *et al.* 1999). The vortices emanating from the LSB have high spanwise coherence (see Burgmann & Schröder (2008), for instance). These highly correlated structures are mostly two-dimensional spanwise vortices. Usually, soon after the formation of these two-dimensional vortices, they start to become distorted and may undergo a complete three-dimensional breakdown (Maucher, Rist & Wagner 1997). To reveal the modes of the flow when a LSB is subjected to external forcing, Michelis (2017), Michelis, Kotsonis & Yarusevych (2018*a*) and Kurelek *et al.* (2018) performed proper orthogonal decomposition (POD) (see Holmes *et al.* (2012), for instance). However, these studies did not explicitly look into the cases where aerofoil tones are generated through a self-sustained mechanism.

Furthermore, previous experimental studies on aerofoil self-noise (McAlpine 1997; Nash *et al.* 1999; Nakano, Fujisawa & Lee 2006; Pröbsting, Serpieri & Scarano 2014; Pröbsting *et al.* 2015) have only performed two-dimensional velocity measurements; as such, they were unable to capture full three-dimensional flow features. On the other hand, previous DNS on aerofoil tones were mostly two-dimensional (Desquesnes *et al.* 2007; Tam & Ju 2012; de Pando, Schmid & Sipp 2014), with the exception of Sanjose *et al.* (2019), who performed a three-dimensional DNS including the open-jet environment. Yet, for the present Reynolds number, a two-dimensional flow is characteristically different from a three-dimensional one (Kraichnan 1967), in that the process of energy cascade can no longer be linked to vortex stretching in the spanwise direction. Hence, studying an inherently three-dimensional flow phenomenon with a two-dimensional DNS can be misleading. Yet, de Pando *et al.* (2014) argued, based on existing experimental measurements, that as the boundary-layer instabilities associated with aerofoil tones are

coherent in the spanwise direction; therefore, the main features of the generation of tones can be assessed by two-dimensional simulations. Moreover, these numerical studies were achieved at Mach numbers much higher than their experimental counterpart. However, if the feedback loop is caused by acoustic disturbances travelling upstream, towards the leading edge, then the flow Mach number becomes an important metric. Nevertheless, a full three-dimensional DNS with a significant span at these Reynolds numbers (~ 0.5–6.0×10^5) and Mach number (~ 0.05) remains computationally prohibitive. Thus, the third objective of the paper is a three-dimensional flow-field measurement and its modal decomposition at low Mach number of 0.05 and low to moderate Reynolds number (based on the chord) of 1.4×10^5, at a geometric angle of attack of $5°$. Furthermore, these measurements have been performed in a unique anechoic and low turbulence intensity environment to decouple aerofoil self-noise from external forcing. No external forcing either acoustic or hydrodynamic is applied, and the problem of self-sustained aerofoil tonal noise is therefore studied.

The choice of the CD aerofoil in the present study comes from its broad range of applications in various modern ventilation and propulsion systems, from high-speed turbofans and compressors to aircraft and automotive low-speed ventilators. Indeed, this aerofoil geometry reduces drag by controlling the turbulent boundary-layer diffusion on its suction side. Therefore, such a study is expected to additionally advance knowledge and understanding not only on aerofoil tones but also on boundary-layer transition, in various low-speed (low Mach number) and low–moderate Reynolds number applications such as small scale fans, ventilation systems, model drones and UAVs. Furthermore, these velocity–pressure data sets will provide a benchmark for validation of future three-dimensional DNS (with a significant span) at this Reynolds and Mach number.

2. Experimental set-up and instrumentation

As mentioned above, to mitigate contamination of the measured signal from external spurious sources, all the measurements for the aerofoil tonal noise case have been carried out in the anechoic open-jet wind-tunnel facility located at the Université de Sherbrooke (UdeS) (Padois *et al.* 2015). The CD aerofoil has a 0.1347 m chord (C), a 0.3 m span, a 4 % thickness-to-chord ratio and a $12°$ camber angle. The aerofoil is equipped with several pinholes, which are located along the chord and span as shown in figure 2. These pinholes are used to measure pressure fluctuations using remote microphone probes (RMP) (Perennes & Roger 1998) and mean static pressure using pressure sensors (see Sanjose *et al.* (2019) for details). In particular, Knowles FG 23329-P07 microphones with a nominal sensitivity of approximately 22.4 mV Pa^{-1} and a dynamic range of 115 dB have been used. These microphones are connected remotely using a 0.5 mm pinhole. Since these microphones are connected remotely, a correction in phase and magnitude is needed. This has been achieved by performing an *in situ* calibration of the RMP (see Jaiswal *et al.* 2020). Lastly, to measure mean wall pressure the pinholes are connected to a capacitance based manometer, which has an accuracy of ± 0.25 % on the reading range.

The CD aerofoil is placed at a $5°$ geometric angle of attack with the help of Plexiglas plates of thickness 4.725 mm laser cut to reduce uncertainty in angle of attack while placing the aerofoil and at the same time giving good optical access. All the measurements are performed at 16 m s^{-1} corresponding to $Re_c = 1.4 \times 10^5$. At these conditions, as reported previously, acoustic tones are heard (Padois *et al.* 2016; Sanjose *et al.* 2019), as shown in figure 1(*b*).
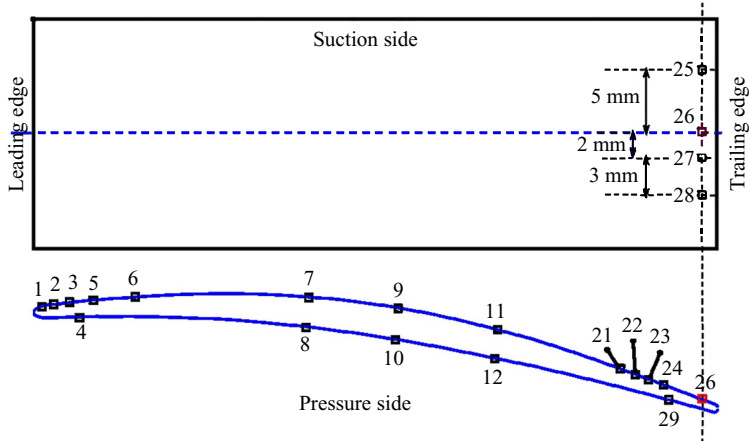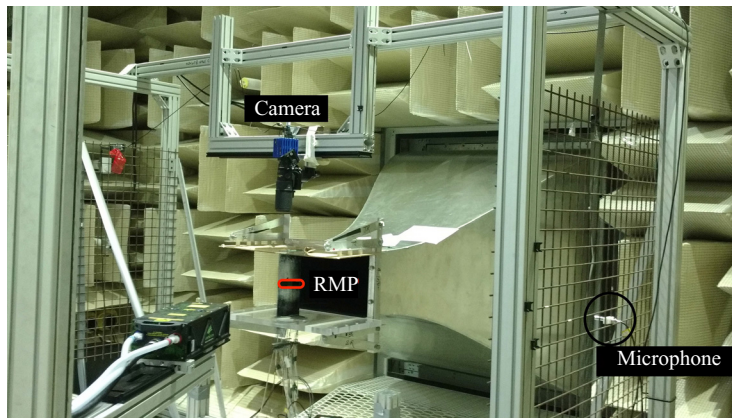
Figure 2. Location of pinholes on the CD aerofoil.

Figure 3. Planar PIV set-up for synchronised velocity–pressure measurements.

2.1. *Synchronised planar particle image velocimetry measurements*

Synchronised velocity–pressure measurements have been performed to reveal the causality between local flow-field disturbances and far-field acoustics. The time-averaged correlation map is expected to reveal the pattern and region of the boundary layer that is responsible for far-field noise. The synchronised measurements are achieved by simultaneously measuring velocity, wall pressure and far-field pressure using particle image velocimetry (PIV), RMP and a 1/2 inch microphone with an integrated circuit piezoelectric, respectively. These measurements are made by placing the laser and its cooling system inside the anechoic wind-tunnel facility. To ensure that the far-field microphone recorded only the aerofoil self-noise, acoustic wedges were placed around the laser-cooling system. Two synchronised measurements were performed on the suction and pressure sides of the aerofoil. The synchronisation between PIV and pressure measurements was achieved using the procedure outlined by Henning *et al.* (2008). Lastly, separate wall-pressure and far-field acoustic measurements were performed without the PIV set-up to confirm the proper noise shielding of the wedges in the above synchronised case.

Parameters	Suction-side boundary-layer measurements (M1)	Pressure-side boundary-layer measurements (M2)
Number of images	4000	2400
Interrogation window (pixel^2)	24×24	16×16
Lenses focal length (mm)	200	200
Field of view (mm)	22.7	19.3
Magnification	0.73	0.855
Digital magnification (pixel mm^{-1})	114	132
Maximum particle image displacement (pixels)	14	13
Acquisition frequency (Hz)	8	8

Table 1. Parameters used for the planar PIV measurements.

2.2. *Planar PIV measurement set-up*

The images for the planar PIV measurements have been acquired with a 5.5 megapixel sCMOS camera. An Evergreen ND:YAG dual pulsed laser was used as the light source. This dual pulse laser can yield up to 200 mJ of energy per pulse. The pulse duration was set to 30 ns. A portable smoke machine was used to seed, which generates a fog of glycerin droplets. The size of these droplets was roughly 1 μm in diameter. The anechoic room was filled with the glycerin droplets, and the images were acquired only when the glycerin droplets were distributed uniformly in the image plane. For the suction and pressure-side measurements, images were acquired at a sampling frequency of 8 Hz. The digital magnification for the suction- and pressure-side measurements was approximately 114 and 132 pixel mm^{-1}, respectively. The time between image pairs was chosen to minimise the relative random error in estimating the particle displacement. Consequently, the free-stream particle displacement for the suction-side and pressure-side measurements was approximately 14 and 13 pixels, respectively.

Images were processed with Lavision's DAVIS 8.4 software using a multigrid iterative window deformation scheme. A total of nine passes was achieved. In the iterative multigrid scheme, an overlap of 75 % and an elliptical weighting (elongated in the mean-flow direction) were used. For the suction-side vector calculations, the initial window size was 96×96 pixels, while the final window size for the suction-side measurement was 24×24 pixels, yielding a spatial resolution of approximately 0.21 mm (a vector pitch of 0.0525 mm). In total, approximately 4000 images were acquired and processed for the suction-side measurements. For the pressure-side measurement calculation, the initial window size was 64×64 pixels, while the final window size for the suction-side measurement was 16×16 pixels, yielding a spatial resolution of approximately 0.12 mm (a vector pitch of 0.04 mm). In total, 2400 images were acquired and processed for the pressure-side measurements.

In all the measurements, an average velocity field has been initially calculated by processing the first 700 images. For the subsequent calculations using the multipass scheme, the average velocity field is used as a predictor for the particle image displacement in the first pass. This increases the overall value of the particle displacement correlation. All the relevant measurement parameters are listed in table 1 for the convenience of the reader.
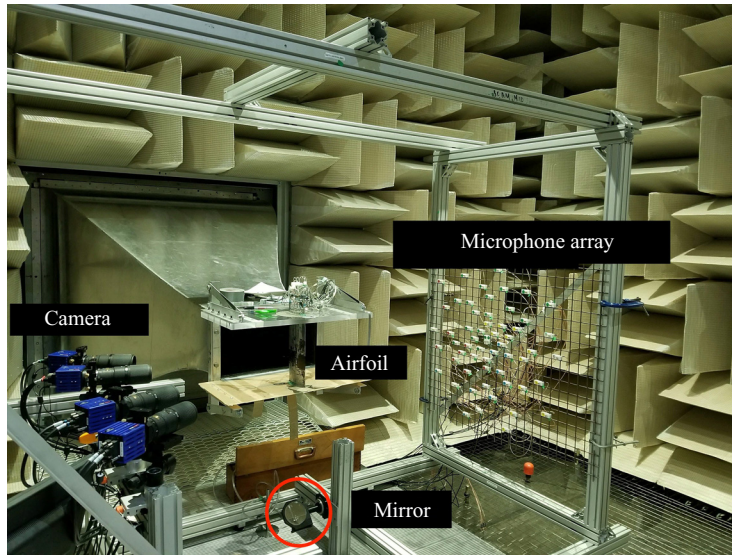
Figure 4. Experimental set-up for the Tomo-PIV measurements and acoustic array.

2.3. *Tomographic PIV set-up*

The tomographic PIV (Tomo-PIV) measurements have been performed using four sCMOS cameras each with a sensor size of 2560×2160 pixels arranged linearly in a side scattering mode to minimise reflections (see figure 4). Since the source region of aerofoil self-noise is near the trailing edge (see Amiet (1976), for instance), the flow measurements were performed in the trailing-edge region. Camera sensors are rotated to align the largest and the smallest sides of the sensor with the spanwise and the streamwise directions of the aerofoil, respectively. The cameras are fitted with AF Nikkor 200 mm $1 : 4D$ lenses to achieve an average optical magnification of 56 pixel mm^{-1}. An ND-YAG dual pulsed laser from Litron Inc (Nano-PIV) was used as a light source, and the volume was generated using Lavision's volume optics module. The energy output was measured to be equal to 385 mJ from laser 1 and 425 mJ from laser 2. The size of the measured volume is approximately 3(streamwise) $\times$ 4(span) $\times$ 0.7(wallnormal) cm^3. Glycerin particles are used as seeding material, and an average physical particle size is estimated to be around 1 μm diameter. All the PIV data have been first processed using Lavision's commercial code DAVIS 8.4. For the processing of the Tomo-PIV data, the images were preprocessed to remove the background noise. The image quality was then improved with further image processing where local nonlinear filtering was used to remove surface reflections and a Gaussian smoothing filter of kernel size 3×3 applied to make the particles appear round and regular. The tomographic image reconstruction step was achieved using the Fast multiplicative algebraic reconstruction technique (Fast-MART) algorithm wherein a 10 simultaneous MART (SMART) iteration is performed followed by nine smoothing operations. Since the source density is estimated to be slightly higher than 0.3, the reconstruction of ghost particles cannot be avoided in the reconstructed field (Novara 2013). To reduce the ghost particle reconstruction, the motion tracking enhancement(MTE) algorithm is used. In total, three MTE iterations are achieved before the final correlation analysis. The first MTE iterations are performed on a coarser grid to save time and also improve the accuracy of the predicted velocity. The last two MTE

Parameters	Values
Volume size (as a fraction of chord length C)	0.3 C (span) 0.25 C (stream) 0.0453 C (wall-normal)
Number of Images	∼1700
Voxel Size (pixel^3)	$24 \times 24 \times 24$
Lenses focal Length (mm)	200
Numerical aperture F	11
Digital Magnification (pixel mm^{-1})	∼56.0
Maximum particle image displacement (pixels)	20
Acquisition frequency (Hz)	10.0

Table 2. Parameters used for the tomographic PIV measurements.

Quantity measured	Uncertainty (95 % confidence)
Tunnel inlet velocity	1 % U_∞
Dynamic pressure Q	0.15 % $\times Q$
Random error mean velocity planar PIV	∼0.73 % U_∞
Random error mean velocity Tomo-PIV	0.0357 % U_∞
Averaging uncertainty $R_{ij} = 0.05$ Planar PIV	3.15 %
Averaging uncertainty $R_{ij} = 0.05$ Tomo-PIV	4.85 %
Averaging uncertainty $\epsilon_{\Theta_{ij}}[\gamma_{ij} = 0.25]$	14.14 %
Averaging uncertainty on autospectra	0.7 dB

Table 3. Uncertainty quantification for various measured quantities.

iterations were made on a finer grid of size $28 \times 28 \times 28$ voxel^3, which is also the size of the final grid. All the correlations are achieved using the direct correlation method. Before the final velocity correlation step, a zero velocity at the wall was applied and the reconstructed volume below the wall masked. These steps are found to improve the near-wall velocity predictions. Finally, the physical size of the voxel of interrogation is approximately 0.5 mm^3 with a vector pitch of 0.125 mm. In total, approximately 1700 images were processed. All the relevant measurement parameters are listed in table 2 for the convenience of the reader.

2.4. *Uncertainty quantification*

Finite recording time in measurements results in statistical spread of the measured quantity. This statistical spread or averaging uncertainty in estimating mean, standard deviation and higher-order statistics depends on the number of independent samples (Benedict & Gould 1996). The present authors (Sanjose *et al.* 2019; Jaiswal *et al.* 2020) and several others have used the finite sampling time in PIV, wall-pressure and far-field acoustic measurements to estimate the averaging uncertainty in the first-, second- and fourth-order statistics. Following the same approach the averaging uncertainty in statistical quantities have been reported in table 3. The first- and second-order statistics are all below 1 % and 5 % respectively. For the quantification of phase velocity (taken from Glegg & Devenport 2017, p. 293), the averaging error ($\epsilon_{\Theta_{ij}}$) in calculating the phase Θ_{ij} between
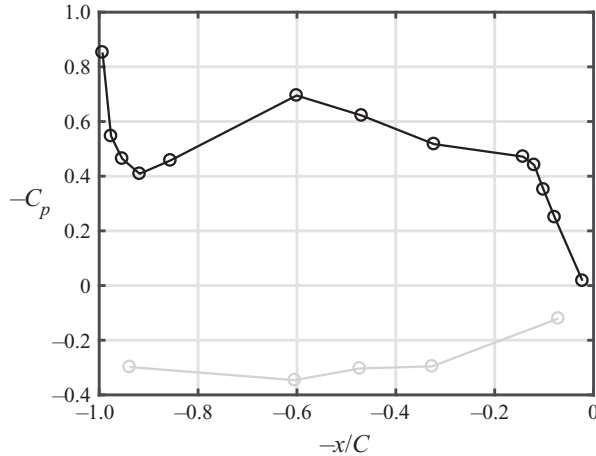
Figure 5. Mean wall-pressure coefficient C_p. Black circle with solid line C_p distribution on the suction side; light grey circle with solid line C_p distribution on the pressure side.

two RMPs, is given by the following equation:

$$\epsilon_{\Theta_{ij}} = \frac{\sqrt{2} \times \sqrt{1 - \gamma_{ij}^2}}{\gamma_{ij}\sqrt{N_s}}, \tag{2.1}$$

where, N_s is the number of independent samples and γ_{ij}^2 is the magnitude squared coherence (MS coherence), while γ_{ij} is simply its square root.

Lastly, table 3 also reports various random errors that are inherent to any PIV measurements (see Ghaemi, Ragni & Scarano (2012), for instance).

3. Wall-pressure analysis

The mean wall-pressure coefficient (C_p) is plotted in figure 5. Here, (x, y) represents the fixed laboratory reference frame at the aerofoil midspan, x being parallel to the jet axis and oriented with the flow, and the origin is taken at the aerofoil trailing edge. A plateau in the value of C_p can be seen at approximately 0.85–0.88 chord (corresponding to the positions of RMPs 21 and 22), indicating a mean-flow recirculation bubble as was shown before by Sanjose *et al.* (2019). On the suction side, the flow encounters a favourable pressure gradient until approximately 0.60 chord. However, the mean wall pressure does not reveal the unsteady nature of the flow past an aerofoil. To reveal this, histograms of C_p are plotted at different locations along the aerofoil in figure 6. Each histogram is computed using Matlab's built-in function histogram. To increase the confidence in estimating the probability density, a moving average filter was used (see Grandemange (2013), for instance). Figures 6(*a*) and 6(*b*) compare the effects of the moving average filter on the distribution. Although the distribution pattern is not substantially altered, the confidence in measurement is improved because averaging reduces measurement noise. Therefore, for the subsequent plots the moving average filter has been retained. On the one hand, from figure 6, the pressure is seen to have a broad distribution from RMP 22 to RMP 24. This broad pressure distribution is the first sign of the flapping of the LSB. On the other hand, the histogram of RMP 21 shows a very narrow distribution, indicating one preferred state of the LSB bubble, perhaps due to the phase locking. Finally, note
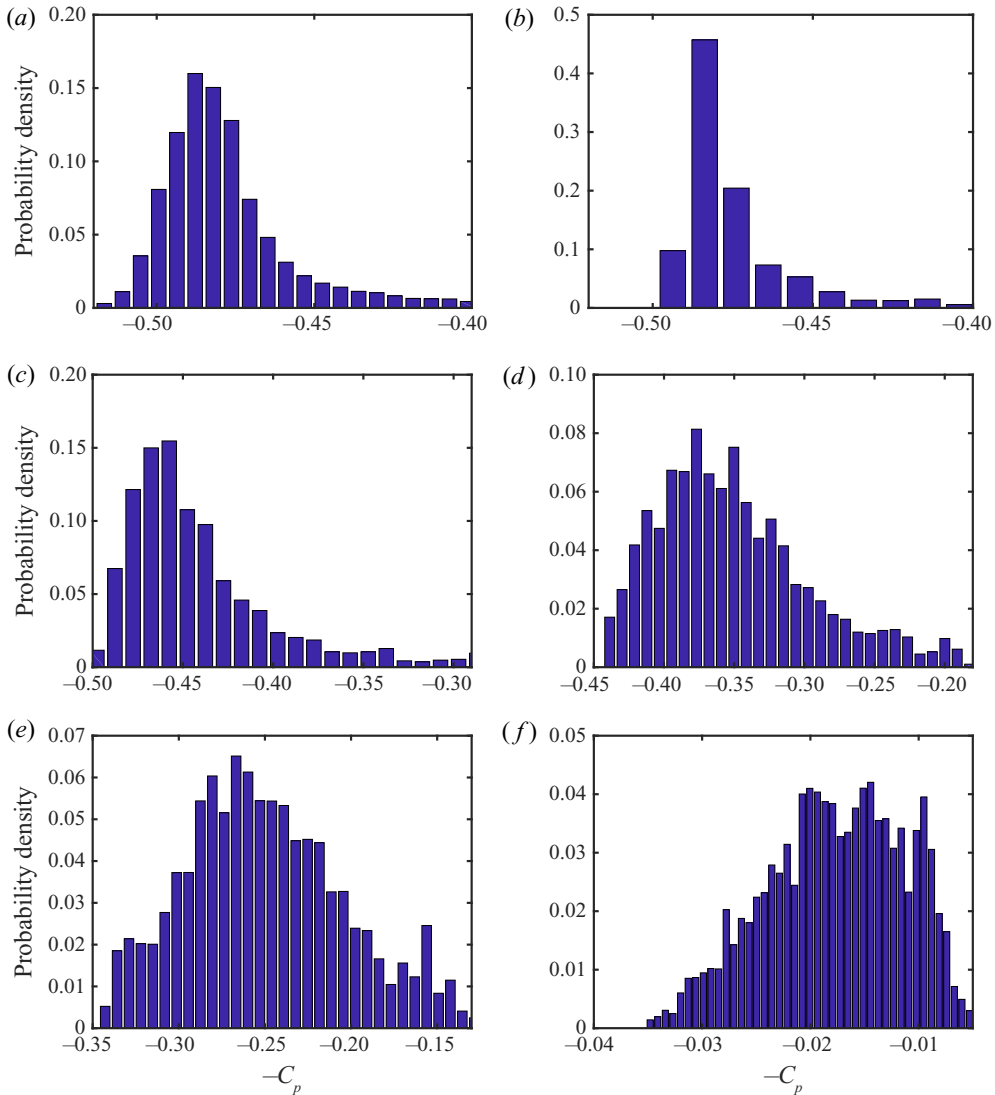
932 A37-10

Figure 6. Probably density function of the loading. (*a*) RMP 21 ($x/C = 0.85$) without moving average filter; (*b*) RMP 21 ($x/C = 0.85$) (with moving average filter); (*c*) RMP 22 ($x/C = 0.88$); (*d*) RMP 23 ($x/C = 0.90$); (*e*) RMP 24 ($x/C = 0.92$); (*f*) RMP 26 ($x/C = 0.98$).

that the probability density function is not only broadening toward the trailing edge but also switching from a unimodal distribution with a single peak to a bimodal distribution, similarly to what is observed for instance in a three-dimensional corner separation in a linear compressor cascade (Gao *et al.* 2015).

The autospectra of the wall-pressure fluctuations are plotted in figure 7. Figure 7(*a*) shows them at the leading edge whereas figure 7(*b*) focuses on the trailing-edge region. The latter autospectra have much higher levels, which is typical of a turbulent boundary layer. The former have levels at least one decade lower with much sharper slopes typical of laminar boundary layers on this aerofoil (Moreau & Roger 2005). For instance, RMPs 1 and 2 show very similar behaviour as was found at the same locations on the same aerofoil
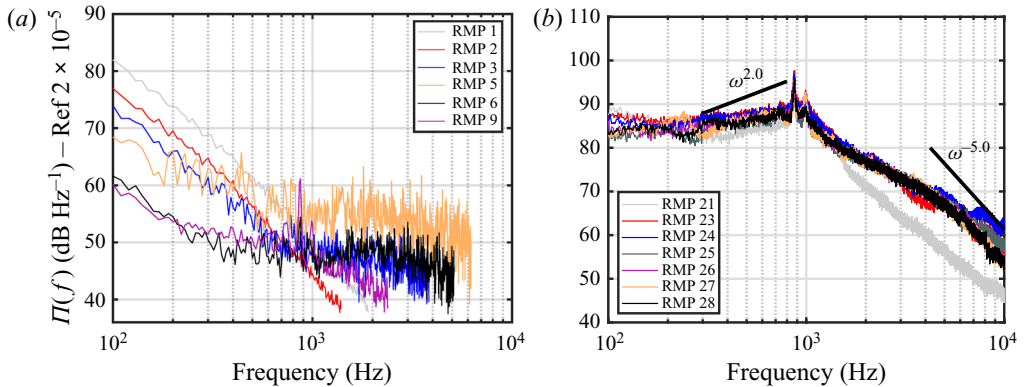
Figure 7. Autospectra of wall-pressure fluctuations on the suction side of the aerofoil placed at $5°$ and 16 m s^{-1}: (*a*) leading-edge and mid-chord sensors (RMPs 1 to 9); (*b*) trailing-edge sensors (RMPs 21 to 28).

at $8°$ angle of attack by Moreau & Roger (2005). However, a high frequency broadband hump (beyond 1 kHz) starts to appear in the wall-pressure spectra from RMP 3 onwards, which suggests the presence of instabilities within the boundary layer. Its peak amplitude is observed near RMP 5 and then starts decaying toward mid-chord, most likely because of the positive mean pressure gradient observed in figure 5 that stabilises the boundary layer and any hydrodynamic instability. Moreover, all autospectra exhibit several discrete peaks superimposed over the broadband signal starting at RMP 3. A clear dominant peak starts emerging at 864 Hz from RMP 5 to the trailing edge (figure 7*b*). Only for RMP locations 1 and 2 are no peaks seen. Thus only a very narrow band of frequency gets amplified beyond RMP 3, resulting in peaks in the wall-pressure spectra. It was conjectured by Tam (1974) that this frequency selection is caused by a feedback loop. These peaks in the wall-pressure spectra are present from 7 % of the chord length until the aerofoil trailing edge. Note that these tones are several decibels (at least 10 to 20 dB) higher than the broadband contribution, a sign of resonance. These findings are in line with the results of Yakhina *et al.* (2020), who also reported that RMPs located close to the leading edge of the aerofoil show amplification in wall-pressure spectra at discrete frequencies, which are equal to that of the tonal noise frequencies. Furthermore, if these flow disturbances are phase locked with acoustic or hydrodynamic disturbances, then large parts of the aerofoil in the streamwise and spanwise directions should be correlated.

To verify the extent of correlation over the suction side of the aerofoil, the magnitude squared coherence (between different RMPs) is plotted in figure 8. Figure 8(*a*) shows that at the tone frequencies large parts of the aerofoil chord are correlated. In fact, RMP 3, located close to the leading edge of the aerofoil, correlates with RMP 26 that is close to the trailing edge, at the principal tone frequency. This substantiates that the feedback loop extends close to the leading edge of the aerofoil. This is consistent with the leading-edge receptivity theory (Saric *et al.* 2002), and wavelength conversion processes seem to take place at the leading edge of the aerofoil in the present case. Similarly, figure 8(*b*) shows that, when the distance between two RMPs is smaller, large bands of frequencies show significant values of magnitude squared coherence. In contrast, at large separation distances (greater than ~ 1–$2 \times \delta_{95}$), the magnitude squared coherence is only significant for a very narrow band of frequencies. Similar results were obtained with the data sets of Yakhina (2017). Note that such high coherence levels at a given frequency over such large distances are only found when a resonance phenomenon such as a feedback loop is
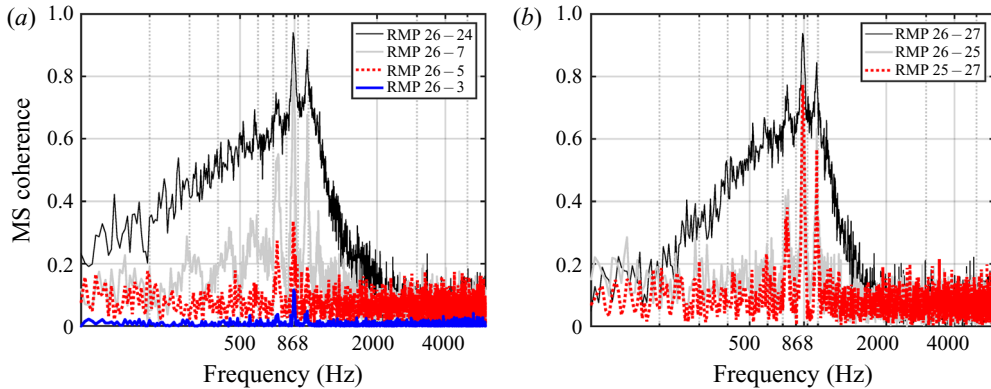
932 A37-12

Figure 8. Magnitude squared coherence: (*a*) coherence for probes in the streamwise direction; (*b*) coherence for probes in the spanwise direction.

present. Indeed, for a fully turbulent flow field, the vortical structures dissipate quickly and consequently the streamwise correlation of wall-pressure fluctuations remain low and drops quickly with distance (see for instance figures 10 and 11 in Moreau & Roger 2005).

A RMP captures both acoustic and hydrodynamic pressure fluctuations. The latter, being the dominant ones in terms of magnitude, can mask the former. Nevertheless, the acoustic fluctuations can travel vast distances with small attenuation in any direction. In comparison, the hydrodynamic turbulent fluctuations undergo a rapid attenuation and are convected with the flow. This property can be used to distinguish between acoustic and hydrodynamic fluctuations, for example, when the RMPs are separated by considerable distance ($\sim$6–10 $\times \delta_{95}$).

To establish the nature of the feedback loop, the convection velocities are calculated. The convection velocity can be calculated either by performing the cross-correlation on a filtered (band-passed) signal (see Willmarth & Wooldridge (1962), for instance) or by calculating the derivative of the unwrapped phase for the range of frequency of interest (Moreau & Roger 2005; Del Álamo & Jiménez 2009). The latter is shown between RMPs 21 and 26 in figure 9. The black solid line shows information travelling in the downstream direction, while the red dashed line shows information travelling in the upstream direction. The existence of such waves travelling in both directions is a necessary condition for a feedback loop. Two other changes of phase occur at side peaks, i.e. $\sim$738 Hz and $\sim$990 Hz. They all yield propagation velocities close to the speed of sound.

To confirm this result and to obtain a more accurate estimate of propagation speed, the convection velocity has also been calculated using the cross-correlation approach. This procedure is encapsulated below:

 (i) Correct the individual RMP signals for any distortion in phase (see Zambonini & Ottavy (2015), for instance).
 (ii) Use zero-phase digital band-pass filtering to retain only the frequency range of interest.
 (iii) Calculate the cross-correlation between the two filtered signals to determine the time lag for the maximum value of correlation.
 (iv) Calculate the convection velocity by dividing the separation length by the time lag.

Nevertheless, even a small change in phase (due to the calibration procedure of the RMP) can lead to a significant error in convective velocity. To minimise the relative
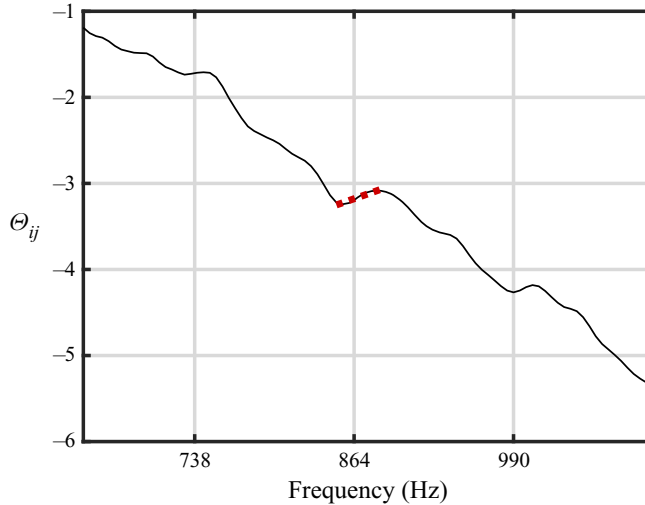
Figure 9. Phase of wall-pressure fluctuations between RMPs 21 and 26: dashed red line highlights the slope change at the dominant tone frequency.
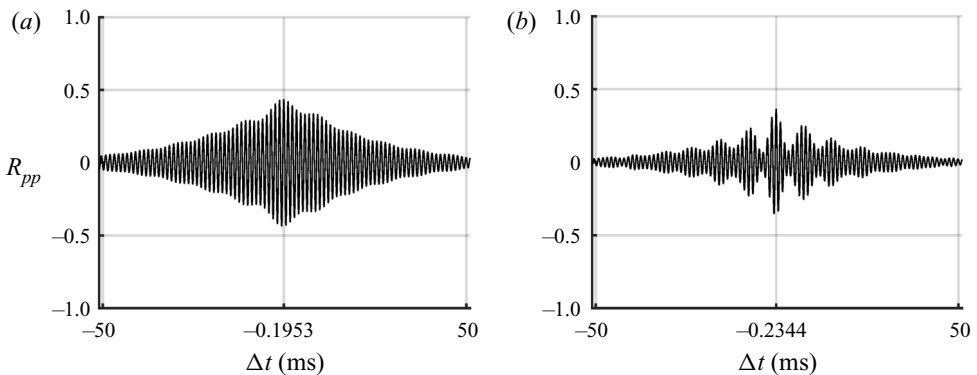

Figure 10. Cross-correlation: (*a*) between filtered (band-passed 650–1050 Hz) signals of RMPs 26 and 9; (*b*) between filtered (band-passed 650–1050 Hz) signals of RMPs 26 and 7.

error, the probes which are separated by large distances are used to calculate the convection velocity. For this reason, the cross-correlation procedure has been found to yield consistent estimates of convection velocity without any data fitting. The results of the cross-correlation analysis in figures 10(*a*) and 10(*b*) show that the maximum cross-correlation coefficient has a negative time delay, implying that the disturbances travel upstream from the trailing edge towards the leading edge of the aerofoil. This unambiguously shows that a feedback loop exists, as shown by many studies in the past (Yakhina *et al.* 2020). Furthermore, the convection speed of these disturbances is close to the acoustic velocity, i.e. 327 m s^{-1} and 309 m s^{-1} for RMPs 26–7 and RMPs 26–9, respectively. This further proves that the feedback loop is acoustic. RMP probes upstream of RMP 7 are not used for the analysis because the value of the correlation is small (figure 8*a*), causing higher uncertainty in the estimation of phase (see (2.1)).
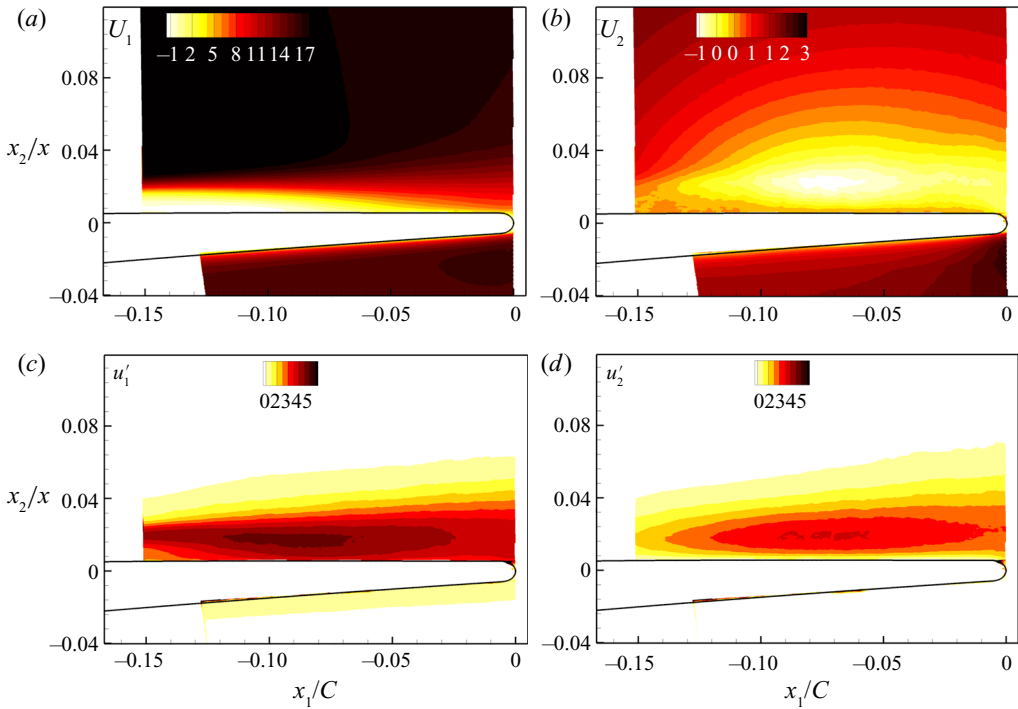
932 A37-14

Figure 11. Velocity field around the aerofoil: (*a*) mean wall-parallel velocity; (*b*) mean wall-normal velocity; (*c*) standard deviation wall-parallel velocity; (*d*) standard deviation wall-normal velocity.

4. Velocity field validation and analysis

To get a more quantitative information about the flow field, figure 11 shows the mean-flow field and the first-order statistics around the trailing edge of the CD aerofoil. A local reference frame (x_1, x_2), normal and tangential to the aerofoil surface at RMP 26, is now used similarly to what Jaiswal *et al.* (2020) defined at an $8°$ geometric angle of attack near the trailing edge of the CD aerofoil. Negative values of mean wall-parallel or streamwise velocity U_1 confirm the presence of a large re-circulation zone near the trailing edge ($\sim 0.85\times$ chord) on the suction side of the aerofoil. According to Nash *et al.* (1999) the existence of the re-circulation region is a necessary condition for the aerofoil tones (Nash *et al.* 1999). This has been recently confirmed by several global stability analyses on two different aerofoils by Wu *et al.* (2021). Furthermore, this separated shear layer undergoes turbulent re-attachment very close to the trailing edge of the aerofoil.

The flow on the pressure side is attached and laminar, as can be seen from low values of turbulent fluctuations in figures 11(*c*) and 11(*d*). This is not surprising since the pressure side encounters a mean favourable pressure gradient (see figure 5), and consequently it creates an unfavourable condition for the growth of any hydrodynamic disturbances at the present moderate Reynolds number. Since the turbulent fluctuations are negligible on the pressure side of the aerofoil (near the trailing-edge region), it appears that the pressure-side boundary layer does not participate in the generation of acoustic tones. However, to confirm this, the causality correlation between far-field acoustic pressure and near-field velocity fluctuations must be evaluated.

To validate the tomographic and planar PIV measurements, the mean and root-mean-square (r.m.s.) velocity profiles are compared at fixed midspan and at discrete

streamwise locations, as shown in figures 12 and 13, respectively. A good comparison is achieved for wall-parallel velocity at all the streamwise locations shown in figure 12. Some discrepancies in measured wall-normal turbulent fluctuations are noticeable close to the wall. This is caused by the finite tomographic angular aperture in the direction of volume reconstruction (Scarano 2012). Lastly, limited spatial resolution results in the three-dimensional modulations (see Ragni *et al.* (2019), for instance), which makes estimation of Reynolds stress less accurate near the wall for the Tomo-PIV measurements. Since the wall-parallel component of the velocity fluctuations decays very slowly (compared with wall-normal velocity fluctuations) near the wall, it requires prohibitively high spatial resolution to avoid any modulations of the measured flow structures. Furthermore, at locations close to the edge of the illuminated volume (RMP 22), this discrepancy is better evidenced. Nevertheless, the comparison between the r.m.s. velocities measured by Tomo-PIV and planar PIV is remarkable when compared with several Tomo-PIV measurements performed in the past on flow over aerofoils. This is partly because of the higher image magnification of the current Tomo-PIV measurements compared with the measurements of the past (see Rafati & Ghaemi 2016, for instance).

Figure 12 also shows values of integral boundary-layer parameters that were calculated using the mean velocity profiles. Higher values of the shape factor H, defined as the ratio of displacement to momentum thickness, between RMPs 21 and 24 confirms the presence of the LSB near the trailing edge of the aerofoil. This is consistent with the observed negative streamwise velocities U_1. In contrast close to the trailing edge, low values of the shape factor (around 1.9) suggest that the flow undergoes a mean turbulent reattachment. This is also evident looking at the fuller boundary-layer profile at RMP 26. This variation of the H-factor in the aft portion of aerofoil also confirms the evolution found in the three-dimensional lattice Boltzmann method DNS (LBM-DNS) (figure 10 in Sanjose *et al.* 2019).

The boundary-layer profiles at RMPs 21 and 22 have inflection points. In fact, they satisfy the necessary condition for the existence of inviscid instability (Fjørtoft 1950; Drazin & Reid 1981). A LSB is known to act as an amplifier of incoming disturbances that enter the laminar separated flow (Theofilis, Hein & Dallmann 2000), and growing unstable modes of Kelvin–Helmholtz-type instability might emerge. These Kelvin–Helmholtz-type instabilities have been reported to exist downstream of a LSB (Watmuff 1999). Kelvin–Helmholtz-type instabilities are marked by large, spanwise vortex rollers, which are predominantly two-dimensional (see Brown & Roshko 1974, for instance). Sanjose *et al.* (2019) also observed these two-dimensional rollers in their three-dimensional LBM-DNS. To confirm the presence of these two-dimensional rollers, the Λ_{ci} criterion (Zhou *et al.* 1999) has been used. Indeed, the velocity gradient tensor can be decomposed in Cartesian coordinates, such that the local streamlines are spanned by the eigenvectors of the velocity gradient tensor. In such a Cartesian coordinate reference frame, the swirling nature of the flow can be characterised by a plane that is normal to the principal axis of vortex stretching or compression. The strength of this local swirling motion is given by Λ_{ci} (Zhou *et al.* 1999). Figure 14 shows the Λ_{ci} criterion, at the same instant, coloured by the streamwise velocity. Large spanwise vortex rollers, which are predominantly two-dimensional, are observed. Similar vortical structures, quiet or intense at different instants, were reported by Sanjose *et al.* (2019). Yet, when comparing with figure 5 in Sanjose *et al.* (2019), the rollers measured over a larger span exhibit a slightly wavier pattern before breaking down, stressing the three-dimensional nature of the transition to turbulence. Indeed, these structures break down into less coherent
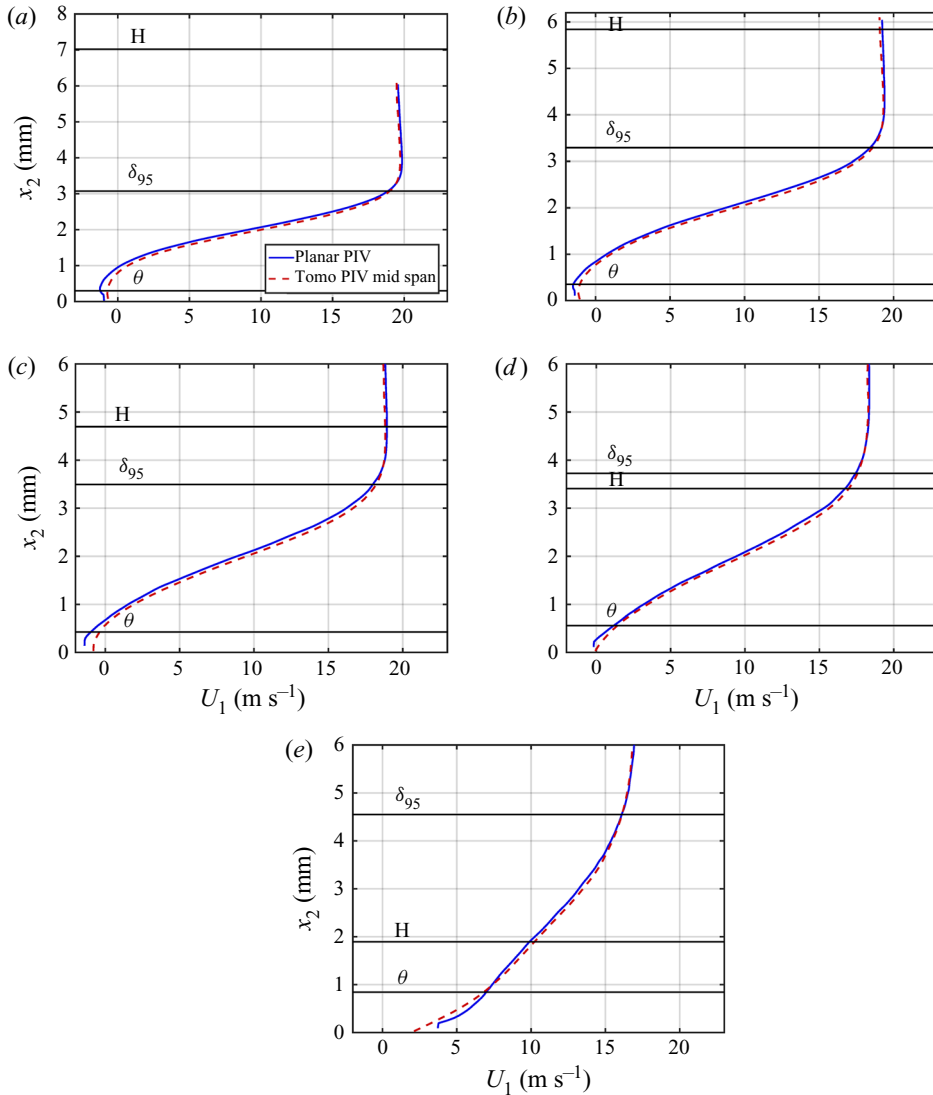
Figure 12. Mean wall-parallel velocity comparison between Tomo- and planar PIV at various streamwise locations: (*a*) RMP 21; (*b*) RMP 22; (*c*) RMP 23; (*d*) RMP 24; (*e*) RMP 26.

three-dimensional vortices near the trailing edge. This observation is further backed by figure 8(*b*), which shows lower values of magnitude squared coherence for large spanwise separation distance, a behaviour typical of fully developed turbulent boundary layers (see Wang *et al.* (2009), for instance).

The transport of streamwise turbulent kinetic energy can be evaluated using the third-order central moments $\overline{u_1'^3}$ and $\overline{u_1'^2 u_2'}$ shown in figure 15 (see Ma, Gibeau & Ghaemi (2020), for instance). Like in the studies of Elyasi & Ghaemi (2019) and Ma *et al.* (2020), the present investigation confirms that the transport of turbulent kinetic energy is carried out by sweep motions (positive $\overline{u_1'^3}$ and negative $\overline{u_1'^2 u_2'}$) in the near-wall region, and farther from the wall by the ejection motions (negative $\overline{u_1'^3}$ and positive $\overline{u_1'^2 u_2'}$). This is true except
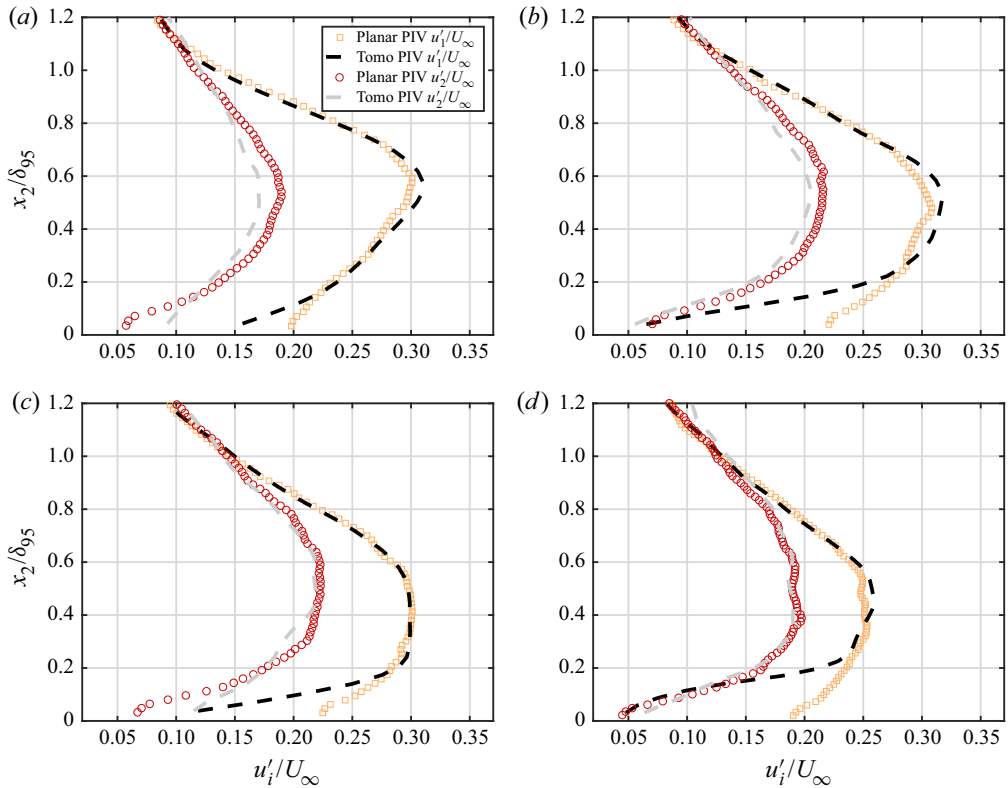
Figure 13. The r.m.s. velocity components u_i' (at midspan) normalised by the inlet velocity U_∞, i.e. 16 m s^{-1}: (*a*) RMP 22; (*b*) RMP 23; (*c*) RMP 24; (*d*) RMP 26.

very close to RMPs 21–22 (0.84–0.87 C) in the near-wall region. An overlap between ejection and sweep motions and the maximum of wall-normal stresses is observed. It has been speculated that this overlap is due to diffusion of turbulent energy by sweep and ejections (Elyasi & Ghaemi 2019). Furthermore, the distribution of ejection events is qualitatively similar to the findings of Elyasi & Ghaemi (2019) and Ma *et al.* (2020) for separated turbulent boundary layers. Yet, the region dominated by the sweep events starts shrinking. Therefore, in the present case the sweep events are much more localised and weakened after the separated boundary layer encounters turbulent reattachment. Lastly, in the present case the regions of ejections and sweeps are located next to each other. Thus the transport of streamwise turbulent kinetic energy is much more efficient here than in the cases considered by Elyasi & Ghaemi (2019), Ma *et al.* (2020).

5. Far-field acoustics

Aerofoil tones consist of distinct peaks in far-field acoustic spectra. As mentioned above, these narrow peaks are intrinsic to the aerofoil tonal noise at moderate Reynolds number based on chord (Pröbsting *et al.* 2015; Yakhina *et al.* 2020), and as such they also exist in the case of the CD aerofoil (see Padois *et al.* (2015), Padois *et al.* (2016) and Sanjose *et al.* (2019), for instance). These observations are confirmed in the present case by the far-field acoustic pressure measurements shown in figure 16. The corresponding power

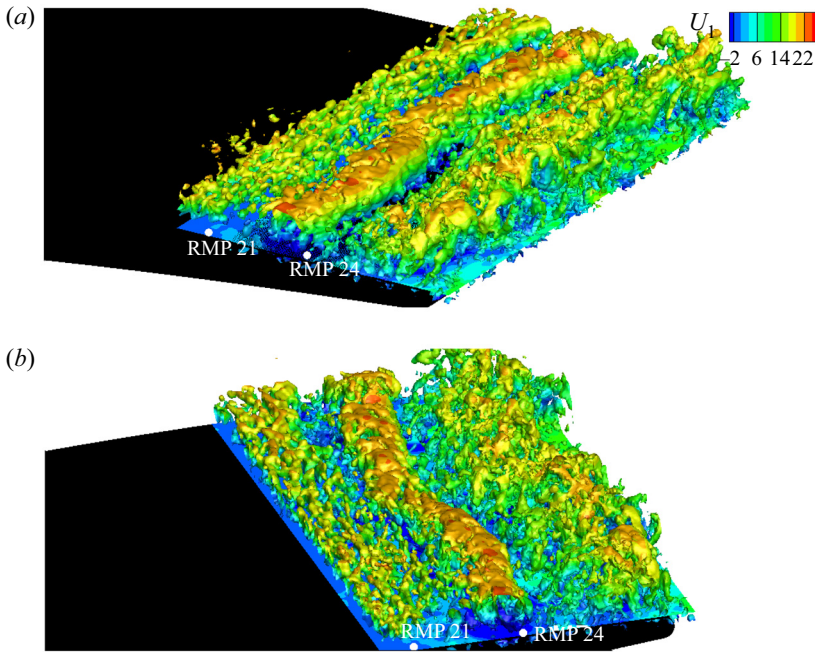Figure 14. The Λ_{ci} criterion coloured with wall-parallel velocity. Note that the span has been truncated to the measurement domain ($0.3C$) to aid visualisation. The figures show the Λ_{ci} criterion at the same instant, but with a different point of view.
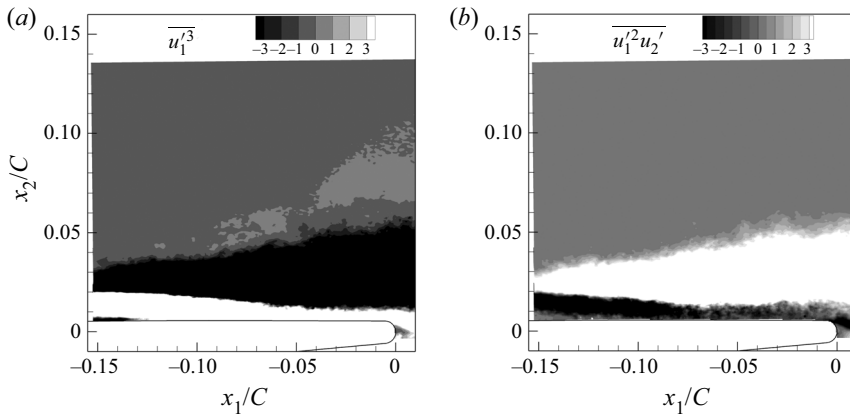

Figure 15. Contours of the third-order central moments $\overline{u_i'^3}$ (at mid-span) in the x_1-x_2 plane: (*a*) $\overline{u_1'^3}$; (*b*) $\overline{u_1'^2 u_2'}$.

spectral density of the far-field acoustic pressure at 1.21 m from the aerofoil trailing edge and at $90°$ from the jet axis is shown in figure 16(*a*). Note that the levels are clearly above the background noise measured without the aerofoil (grey line), over the whole relevant frequency range (up to 10 kHz). A clear dominant tone at 864 Hz emerges over a broadband hump ranging from 300 to 1500 Hz. Two side tones also appear at $\sim$738 Hz and $\sim$990 Hz, corresponding to the above phase inversion in the wall-pressure fluctuations yielding acoustic propagation velocities. Similar spectral features are found at all angular

932 A37-19

locations around the aerofoil, and are very similar to the wall-pressure spectra close to the trailing edge shown in figure 7(b). This is consistent with what Moreau & Roger (2009) found using the extended Amiet model for trailing-edge noise (Amiet 1976; Roger & Moreau 2005). As mentioned in the introduction, the frequency of the primary tone f_S satisfies (1.1), and the frequency separation Δf between the primary and secondary tones is constant (equal to 126 Hz in the present case), as previously observed by Paterson *et al.* (1973) and Arbey & Bataille (1983) for instance. If a feedback loop length L is inferred from (5) in Arbey & Bataille (1983)

$$\frac{L\Delta f}{U_\infty} = 0.37 M_\infty^{-0.15}, \tag{5.1}$$

we obtain $L = 0.55C$, which is beyond mid-chord between RMPs 7 and 9. For these sensor locations a strong tone at f_S was observed in the wall-pressure autospectra (figure 7). In contrast, the linear stability analysis for the same case (see figure 25 in Sanjose *et al.* 2019) predicts the location of the instability to be around $0.78C$ ($L = 0.22C$). The former points to locations with almost zero mean pressure gradient or mild favourable pressure gradient, while the latter corresponds to the location close to the LSB. It is worth mentioning that the assumptions of small perturbations will not hold at locations close to the LSB, as shown below; therefore, the use of linear stability theory (LST) is not strictly valid. Nevertheless, LST is agnostic to the aerofoil geometry used, while (5.1) was obtained through data fitting flows past an NACA-0012 aerofoil. If the length of the feedback loop L and the convection velocity of the flow instabilities U_c are known, then the frequency of the tones can be predicted with the following equation (proposed by Arbey & Bataille 1983):

$$f_n = \frac{U_c}{L}(n + 1/2)\left(1 + \frac{U_c}{a_\infty - U_\infty}\right)^{-1}. \tag{5.2}$$

If L is estimated with (5.1) and U_c taken as the convection velocity of the flow instability ($\simeq 10$ m s^{-1}), (5.2) yields the following frequencies 718, 848 and 979 Hz, close to the experimental ones. If L predicted by LST is used instead, the following frequencies 487, 813 and 1138 Hz can be obtained, which clearly discards such a feedback loop length. Yet, the constant 0.37 in (5.1) might not be more valid than the one in (1.1) for the CD aerofoil, and a longer feedback loop length L extending all the way to RMP 5 in the leading-edge region ($\simeq 0.8C$), where the first strong tone at f_S appears, could be more appropriate and consistent with the aforementioned wall-pressure fluctuations. This leads to the following frequencies 762, 852 and 942 Hz, again close to the experimental ones. Nevertheless, as already mentioned in the introduction, it should be emphasised that all these simplified models rely on strong assumptions such as constant convection velocities and do not provide much physical insight into the physical mechanisms at stake such as the vortex dynamics that yields the observed acoustic signature. Moreover, given the uncertainty on the values input in (5.1) and (5.2), it is also impossible to clearly choose between the two proposed scenarios (mid-chord or leading-edge region).

Figure 16(b) shows the directivity pattern of the far-field acoustic pressure at the principal tone frequency (864 Hz). A dipolar nature of the acoustic tones is confirmed. The noise radiation is principally along the jet axis. Small asymmetry is attributed to the aerofoil camber and to the fact that the aerofoil is placed at a non-zero angle of attack.

However, since acoustic spectra are time-averaged quantities, they cannot reveal the intermittent character of aerofoil tonal noise. Thus, to characterise unsteady behaviour of aerofoil tonal noise, a wavelet transformation (Farge 1992) was carried out on the far-field microphone signal. The continuous wavelet transform was performed using a derivative of
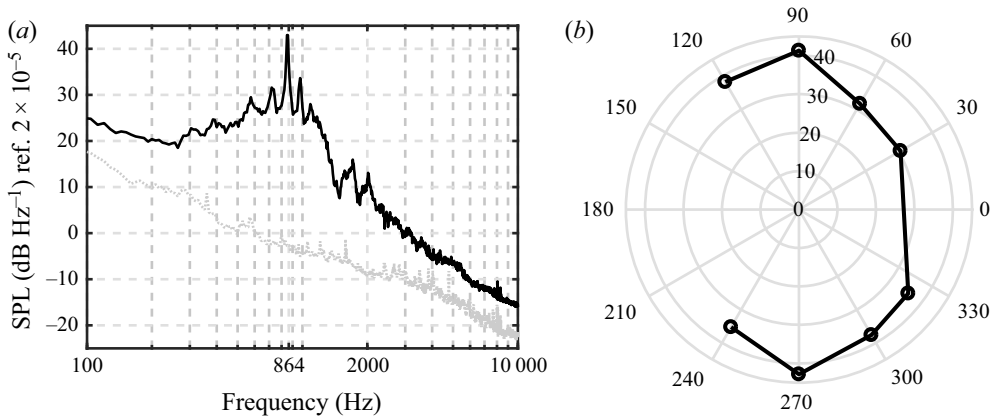
Figure 16. Far-field acoustic measurements at 1.21 m from the aerofoil, and 90° from the jet axis: (*a*) ———— (black) sound pressure level measured with the aerofoil, - - - - - - (grey) background sound pressure level measured without the aerofoil; (*b*) directivity plot at the principal tone frequency at 864 Hz.
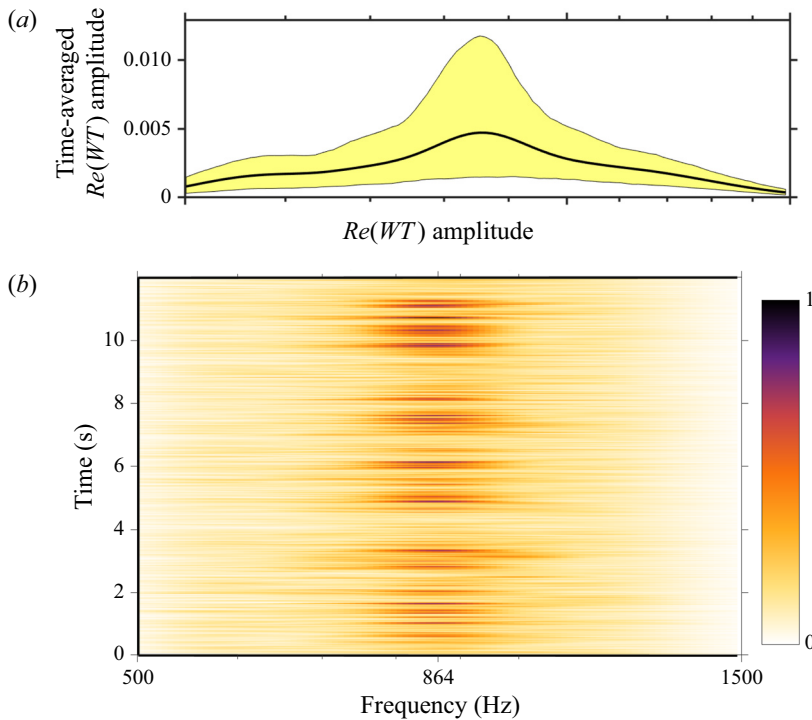

Figure 17. Narrow band frequency–time analysis using wavelet transform of far-field acoustic pressure measured by a microphone, which is placed at 1.21 m from the aerofoil and 90° from the jet axis.

Gaussian wavelet. Figure 17 shows the wavelet transform of a single microphone pressure signal. The tonal noise shows strong modulation in frequency and amplitude. Based on the works of Padois *et al.* (2016), the present tonal noise case falls under the second regime of laminar boundary-layer instability noise, which is characterised by a more intermittent occurrence of the principal tone. This is also consistent with the results found
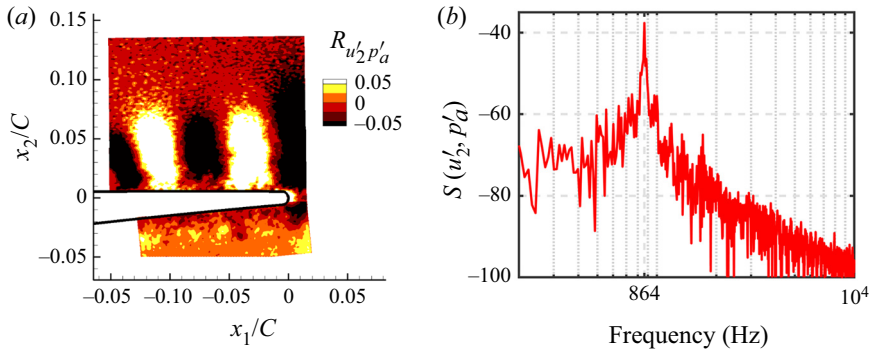
Figure 18. Causality analysis between the near-field wall-normal velocity fluctuations and the far-field acoustic pressure: (*a*) causality correlation $R_{u'_2 p'_a}(\boldsymbol{x}, t)$; (*b*) cross-power spectral density of the causality correlation $S_{u'_2 p'_a}$.

in the three-dimensional LBM-DNS (figure 15 in Sanjose *et al.* 2019). It also confirms the aforementioned strong nonlinearity close to the LSB.

6. Causality analysis

To identify the boundary-layer instability responsible for aerofoil tones, causality correlation between boundary-layer disturbances and far-field acoustic pressure has been performed. The causality correlation can be estimated using Pearson's correlation coefficient. However, it requires choosing of an appropriate metric to quantify the near-field source term. According to Amiet's theory and its extension (Amiet 1976; Roger & Moreau 2005), wall-pressure fluctuations are the noise source for the far-field acoustic pressure, justifying the above shape similarity of the respective spectra. However, only the near-field velocity data are provided by PIV. Among the various velocity components, the wall-normal velocity fluctuations are the principal drivers of wall-pressure fluctuations (see Jaiswal *et al.* (2020), for instance). Therefore, the latter can be used as a source term in the causality study. Pearson's correlation coefficient $R_{u'_2 p'_a}(\boldsymbol{x}, t)$ is then defined as

$$R_{u'_2 p'_a}(\boldsymbol{x}, t) = \frac{\overline{u'_2(\boldsymbol{x}, t) p'_a(\boldsymbol{x}, t + t_f)}}{\overline{u'_2(\boldsymbol{x}, t)} \times \overline{p'_a(\boldsymbol{x}, t + t_f)}}, \tag{6.1}$$

where t_f is the time of flight or the time taken by the acoustic disturbances to arrive at the far-field microphone location, and $\overline{u'_2(\boldsymbol{x}, t)}$ is the standard deviation of the wall-normal velocity. Finally, p'_a is the far-field acoustic pressure, which is recorded using a single microphone placed normal to the aerofoil at midspan (see figure 3).

Figure 18 shows Pearson's correlation coefficient that is referred to as the causality correlation from now on, as it relates the cause and effect of the noise. The causality correlation $R_{u'_2 p'_a}(\boldsymbol{x}, t)$ shows several regions of negative and positive correlation regions/lobes. These lobes of negative and positive correlation extend beyond the boundary-layer thickness, and are reminiscent of the Kelvin–Helmholtz modal shape identified numerically by Sanjose *et al.* (2019), who performed a spectral POD analysis.

The highest value of the correlation is achieved slightly upstream of the trailing edge. This is expected because the trailing-edge noise is caused by the scattering of vortices at the trailing edge (Howe 1978; Roger & Moreau 2005). Furthermore, the maximum correlation coefficient between the upwash velocity and the far-field acoustic disturbance

is negative, implying a negative phase between the two quantities. The distance between the negative and positive lobes of value $R_{u'_2 p'_a}(\boldsymbol{x}, t)$ is equal to half the wavelength of the principal tone frequency. In order to determine the wavelength of the principal tone frequency, the convection speed near the trailing edge is calculated. This is done using the time resolved wall-pressure data. The relation between spacing of the correlation pattern and principal tone frequency becomes more obvious if one moves to the Fourier domain. The absolute value of Fourier transform of the causality correlation ($S_{u'_2 p'_a}$) is plotted against frequency in figure 18(*b*). A peak at the principal tone frequency reinforces the relation between principal tone frequency and spacing of the correlation pattern. Since in the present case the Kelvin–Helmholtz modal pattern is obtained using causality correlation, it can be unambiguously concluded that the Kelvin–Helmholtz-type instability is responsible for the present acoustic feedback loop, yielding the sharp intermittent aerofoil tonal noise.

In stark contrast to the patterns seen on the suction side, no discernible pattern can be seen on the pressure side of the aerofoil from the $R_{u'_2 p'_a}(\boldsymbol{x}, t)$ plot. As a word of caution to the reader, slightly higher values of $R_{u'_2 p'_a}(\boldsymbol{x}, t)$ on the pressure side are an artefact of dividing $R_{u'_2 p'_a}(\boldsymbol{x}, t)$ by close to zero values of u'_2, as shown in figure 11(*d*). Thus, it can be concluded that the pressure-side events do not participate in the far-field acoustic tone generation. Desquesnes *et al.* (2007) had hypothesised that the amplitude modulation in far-field pressure fluctuations can be attributed to the coupling between the suction- and pressure-side disturbances. However, the pressure side of the CD aerofoil at this particular flow condition is not only laminar (figure 11) but also does not correlate with far-field acoustic pressure (figure 18). Therefore, the coupling between pressure- and suction-side disturbances is not a necessary condition for amplitude modulation, as already stated by Pröbsting (2015) for the NACA-0012 aerofoil. This has also been recently confirmed by a global stability analysis on two different aerofoils including the present CD aerofoil by Wu *et al.* (2021). Furthermore, the phase locking between near-field sources and the far-field acoustic pressure causes periodic shedding of coherent structures from the LSB (Pröbsting 2015). Therefore, plotting the two-point correlation of the wall-normal velocity fluctuations (figure 19) produces the same pattern of negative and positive regions. Figure 19 also suggests that the aerofoil tones are the result of a two-dimensional instability mode, which is the goal of the next section.

7. Proper orthogonal decomposition

To unravel the modes of the flow present in such a self-sustained oscillating flow, POD has been used. One of the advantages of POD over linear stability studies employed in the past (see McAlpine (1997), for instance) is that, unlike the latter, POD does not invoke the restrictive assumption of linearity or any assumptions on the magnitude of the disturbances. In the present study, POD has been performed using the method of snapshots algorithm developed by Sirovich (1987). The reader is referred to Holmes *et al.*'s (2012) monograph for details. For the planar PIV case, 800 snapshots of synchronised microphone-PIV measurements have been recorded and processed. The in-house POD algorithm was implemented in Matlab. To validate and test its robustness, the POD results are compared with that obtained using DAVIS (Lavision's commercial software) in figure 20. An excellent agreement between the energy content of these two implementations for the first 100 modes can be seen.
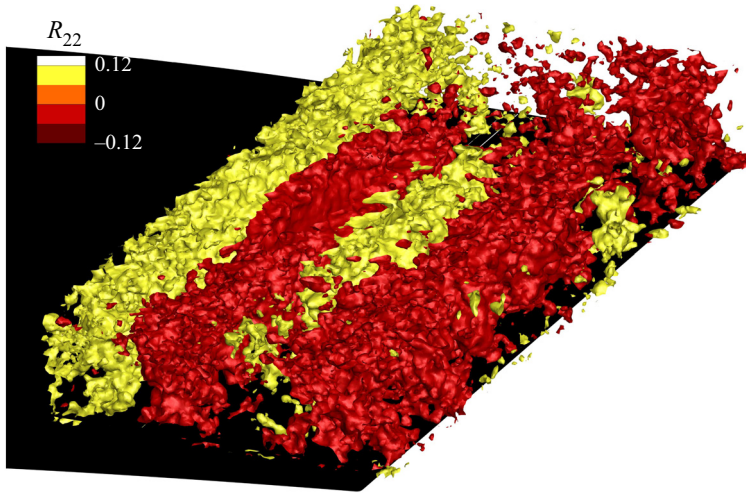
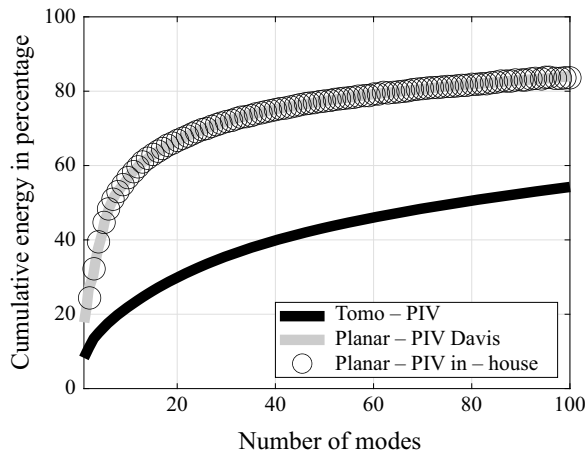Figure 19. Two-point wall-normal velocity correlation for a fixed point located 1 mm from the wall at RMP 22.

Figure 20. Cumulative energy of the first 100 modes.

Figure 20 shows that the first 15 modes account for approximately 60 % of the total kinetic energy. To reveal the spanwise behaviour of the POD modes, the Tomo-PIV data have been used. To get a complete three-dimensional picture, 800 snapshots from the Tomo-PIV measurements have been used for the POD analysis. The cumulative energy distributions of the modes from the Tomo-PIV measurements are also shown in figure 20. It can be noticed that, for the same flow, the cumulative energy distribution is lower compared with the planar PIV. This is not surprising because the flow appears to be homogeneous in the spanwise direction (see figure 19). To quantify the turbulence kinetic energy of homogeneous turbulence, a large number of modes is required (see Glegg & Devenport (2001), for instance). However, planar PIV measurements have been done uniquely in the wall-normal direction, where the turbulence is inhomogeneous due to the wall blocking (Jaiswal *et al.* 2020). Consequently, in Tomo-PIV measurements, a higher
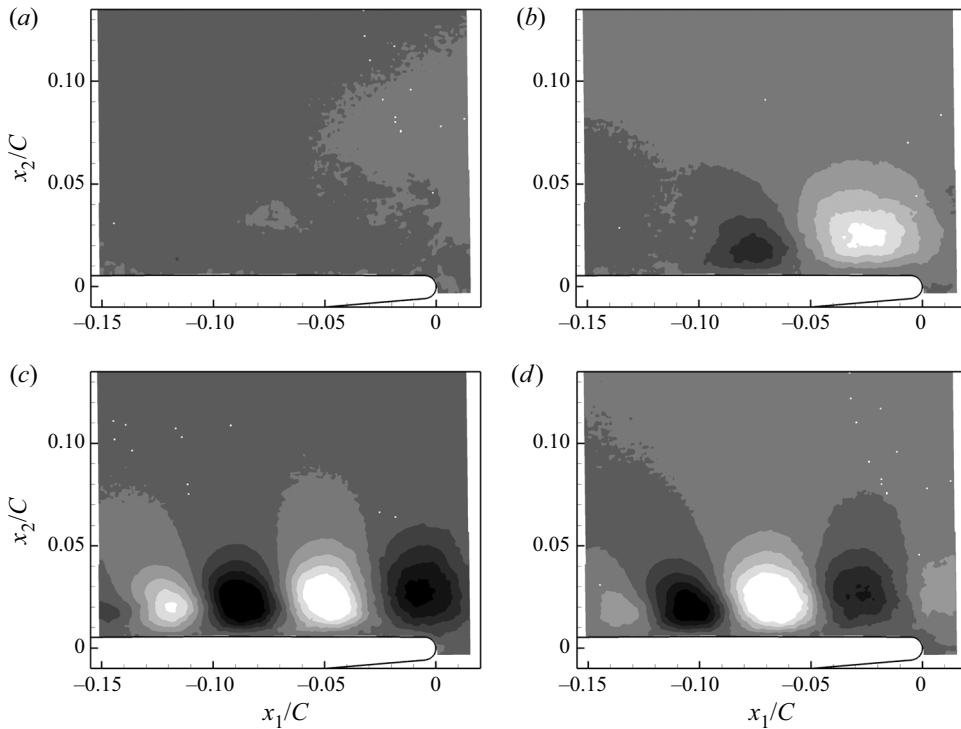
Figure 21. Wall-normal component of the POD spatial eigenfunctions Φ_i^2 in the x_1-x_2 plane: (*a*) mode Φ_1^2; (*b*) mode Φ_2^2 ; (*c*) mode Φ_3^2 ; (*d*) mode Φ_4^2.

number of modes is required to quantify the turbulence kinetic energy compared with the planar PIV case.

Figures 21 and 22 show the first eight modes of the wall-normal velocity fluctuations. The modes of the wall-normal velocity fluctuations are especially useful because the wall-normal velocity fluctuations are directly linked to trailing-edge noise compared with wall-parallel velocity fluctuations (Jaiswal *et al.* 2020). In figure 21 we can clearly see that the modes Φ_3^2 and Φ_4^2 form modal pairs since they are almost perpendicular to each other and they contain almost equal energy. These modes are not perfectly orthogonal because they are affected by the stochastic nature of turbulence. The modal shape is similar to what was obtained from causality correlation analysis in figure 18(*a*). Furthermore, the wavelength of these modes (Φ_3^2 and Φ_4^2) is equal to the principal tone frequency, which classifies them as normal modes. It is interesting to note in the present case that the normal modes of aerofoil tones are not the most energetic ones.

The POD modes from Tomo-PIV data are plotted in figure 23, which shows that the first modal pair (3 and 4) is essentially two-dimensional. These modes appear to be the trace of the main two-dimensional rollers seen in figures 14 and 19. Furthermore, these modes are present throughout the measurement volume, i.e. until the near wake region. Modes 6 and 7 appear to be a result of spanwise modulation of modes 3 and 4, respectively. The two-dimensionality of these tonal noise modes (modes 3 and 4) suggests any changes in the boundary condition along the span of the aerofoil will mitigate the aerofoil tone. Indeed, reduction in tone amplitude was reported in the experimental investigation of Moreau
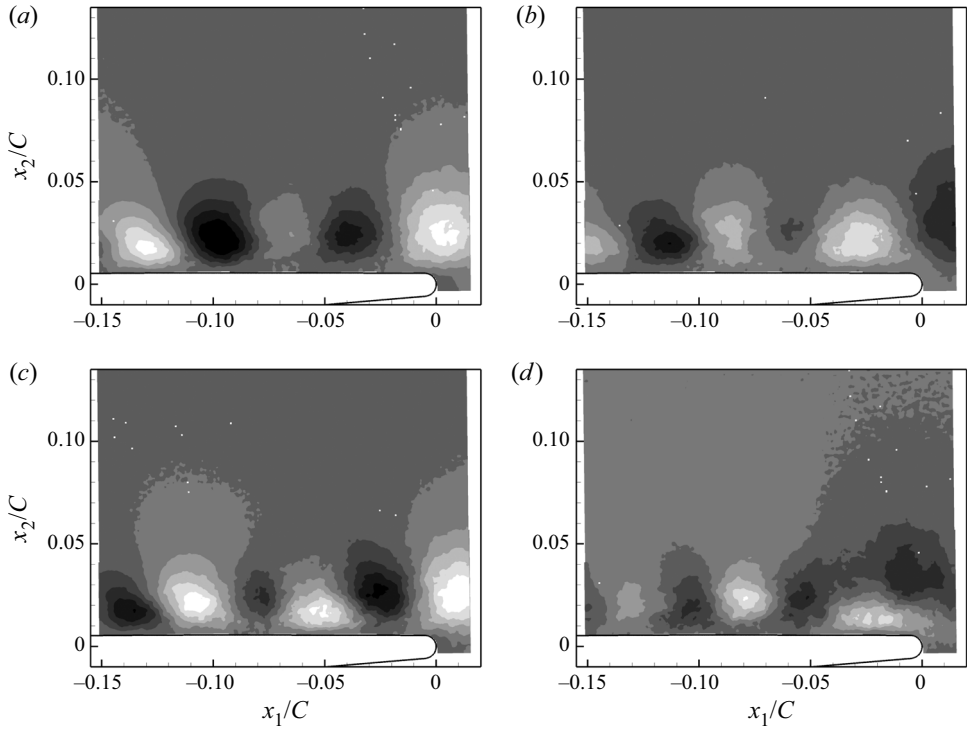
Figure 22. Wall-normal component of the POD spatial eigenfunctions Φ_i^2 on the x_1-x_2 plane: (*a*) mode Φ_5^2; (*b*) mode Φ_6^2 ; (*c*) mode Φ_7^2; (*d*) mode Φ_8^2.
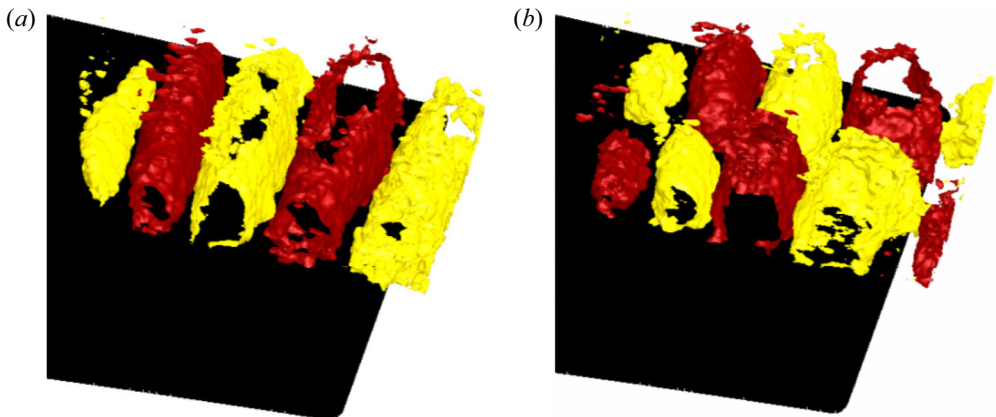

Figure 23. Wall-normal component of the convective POD spatial eigenfunctions (*a*) Φ_3^2 and (*b*) Φ_6^2 in the Tomo-PIV volume. The amplitudes have been normalised by the maximum value of the spatial eigenfunctions.

et al. (2016), who used a modular aerofoil instead of a single-block aerofoil. The gap or the kapton film at the junctions created the spanwise disruption in this case.

At this point, it is instructive to compare the present case with the one where the LSB is excited externally. For example, Kurelek *et al.* (2018) found significant changes in the LSB length and boundary-layer transition when the flow is exited externally with

acoustic disturbances. Furthermore, Kurelek *et al.* (2018) also performed a POD analysis, and the two modal pairs they obtained look very similar to the present case. The only difference being the order of the modal pairs and their energy content, both of which are higher in Kurelek *et al.*'s (2018) study. Another important distinction between the present study and that of Kurelek *et al.* (2018) and Michelis *et al.* (2018*a*) is that, unlike in Kurelek *et al.* (2018) and Michelis *et al.* (2018*a*), no irregular modulation of disturbances (modes 6 and 7) in the spanwise direction is observed. This regular spanwise modulation also implies that a single geometrical discontinuity in span will not be enough to completely suppress the acoustic tones, again corroborating the findings of Moreau *et al.* (2016).

As a LSB is subjected to natural and periodic excitation, a variation in its streamwise and spanwise wavelength is observed (Michelis *et al.* 2018*a*). Michelis *et al.* (2018*a*) also found that, when vortex shedding is locked to the excitation frequency, spanwise deformations diminish and the structures break up further downstream. Given that in the present case the CD aerofoil generates tonal noise that has an amplitude and a frequency modulation, the spanwise modulation of the disturbance (modes 6 and 7) can be most likely linked to the observed modulation amplitude of the tonal noise. This is also consistent with Amiet's model and its extension (Amiet 1976; Roger & Moreau 2005) that show that the far-field acoustic spectra are directly proportional to the spanwise correlation length of the wall-pressure fluctuations, and justifies the good agreement reported by Moreau & Roger (2009) for a similar flow regime with tonal noise (see figure 9 and the case at $-5°$ in figure 15(*a*) in Moreau & Roger 2009).

8. Conclusion

A comprehensive experimental investigation of aerofoil tones has been carried out for a CD aerofoil at low Mach number of 0.05 and low-to-moderate Reynolds number (based on chord) of 1.4×10^5 at a low geometrical angle of attack of $5°$, for which intermittent tonal noise had been reported previously. Microphones have been used to quantify near-field wall-pressure noise sources and far-field acoustic pressure. Synchronised detailed flow measurements using planar and Tomo-PIV have been performed to yield the velocity field.

Large parts of the aerofoil chord and span exhibit high correlations of wall-pressure fluctuations with strong peaks in the auto-spectra at the tonal noise frequency (at least 10 dB above the broadband noise level). The resonance and the causality implied by these wall-pressure measurements also establish the existence of an acoustic feedback loop. Indeed, for the remote microphone probes separated by a significant geometrical distance, disturbances travel upstream at near sonic speeds ($\sim$ Mach 1), giving compelling evidence for the presence of acoustic feedback. Furthermore, these acoustic disturbances can travel far upstream to locations near the leading edge and persist even in the presence of a favourable pressure gradient. This does not support the hypothesis of Arbey & Bataille (1983) that the acoustic feedback loop will be closer to the aerofoil mid-chord. Nevertheless, it is consistent with the analytical works of Goldstein (1983) and the recent experimental evidence provided by Pröbsting & Yarusevych (2021) in that acoustic disturbances travelling upstream enter the leading-edge region of the aerofoil.

The pressure side of the CD aerofoil is not only laminar (figure 11) but also does not exhibit any coherent structure correlated with the far-field acoustic pressure (figure 18). Therefore, the coupling between pressure- and suction-side disturbances is not a necessary condition for amplitude modulation, as already stated by Pröbsting (2015) for the NACA-0012 aerofoil and found by a global stability analysis on two different aerofoils by Wu *et al.* (2021). Therefore, amplitude modulation requires neither a communication

between the two sides of the aerofoil nor a transition to turbulence on the pressure side, the latter argument being used by Pröbsting (2015) to negate Desquesnes *et al.*'s hypothesis.

The far-field acoustic signals analysed with wavelet transform show that far-field acoustic disturbances undergo significant amplitude and frequency modulation. The acoustic measurements corroborate the findings of Desquesnes *et al.* (2007), Padois *et al.* (2016), Yakhina (2017) and Pröbsting (2015). Pearson's causality correlation was calculated between near-field wall-normal velocity fluctuations and far-field acoustic measurements, and gives rise to the Kelvin–Helmholtz-type modal structure. Furthermore, large two-dimensional roller structures reminiscent of a Kelvin–Helmholtz-type instability are also seen, confirming most of the findings of the three-dimensional DNS by Sanjose *et al.* (2019). POD analysis shows that these flow structures are the most dominant convective modes having two-dimensional patterns. Compared with forced cases (Kurelek *et al.* 2018; Michelis *et al.* 2018*a*), the convective POD modes have lower energy content. Higher convective modes (modes 6 and 7 in the present case) appear to be a result of spanwise modulation of the dominant convective modes. Compared with the forced cases (Kurelek *et al.* 2018; Michelis *et al.* 2018*a*) the modulation of disturbances appears to be more regular. This modal structure can explain why, when using a modular aerofoil, Moreau *et al.* (2016) measured a reduction in aerofoil tonal noise magnitude and not a total elimination of aerofoil tones. This also confirms that two-dimensional simulations cannot fully assess the main features of aerofoil tones, as suggested by Tam & Ju (2012) and de Pando *et al.* (2014). Trailing-edge serrations or liner-type porous appendages both create modulations in span, and have been successfully used to mitigate aerofoil tones in the past (Moreau *et al.* 2016; Gelot & Kim 2020).

Declaration of interests. The authors report no conflict of interest.

Data availability statement. Raw data of Tomo-PIV were processed at the Compute Canada's HPC center. Derived data supporting the findings of this study are available from the first author upon reasonable request.

Author ORCIDs.
- Prateek Jaiswal https://orcid.org/0000-0002-5240-9911;
- Stéphane Moreau https://orcid.org/0000-0002-9306-8375.

REFERENCES

AMIET, R.K. 1976 Noise due to turbulent flow past a trailing edge. *J. Sound Vib.* **47** (3), 387–393.

ANDAN, A.D. & LEE, D.-J. 2018 Effect of external acoustic excitation on NACA0015 discrete tonal noise. *Appl. Acoust.* **141**, 374–381.

ARBEY, H. & BATAILLE, J. 1983 Noise generated by airfoil profiles placed in a uniform laminar flow. *J. Fluid Mech.* **134**, 33–47.

ARCONDOULIS, E., DOOLAN, C.J., ZANDER, A.C. & BROOKS, L.A. 2013 An experimental investigation of airfoil tonal noise caused by an acoustic feedback loop. In *Proceedings of Acoustics 2013 – Victor Harbor*, 17-20 November 2013, Victor Harbor, Australia.

ARCONDOULIS, E., LIU, Y. & XU, P. 2019 An investigation of the facility effects on NACA 0012 airfoil tonal noise. *AIAA Paper* 2019-2607.

ATASSI, H.M. 1984 Feedback in separated flows over symmetric airfoils. *AIAA paper*-84-2297.

BENEDICT, L.H. & GOULD, R.D. 1996 Towards better uncertainty estimates for turbulence statistics. *Exp. Fluids* **22** (2), 129–136.

BROOKS, T.F., POPE, D.S. & MARCOLINI, M.A. 1989 Airfoil self-noise and prediction. *Tech. Rep.* NASA-RP-1218. NASA.

BROWN, G.L. & ROSHKO, A. 1974 On density effects and large structure in turbulent mixing layers. *J. Fluid Mech.* **64** (4), 775–816.

BURGMANN, S. & SCHRÖDER, W. 2008 Investigation of the vortex induced unsteadiness of a separation bubble via time-resolved and scanning PIV measurements. *Exp. Fluids* **45** (4), 675–691.

CHONG, T.P. & JOSEPH, P. 2012 "Ladder" structure in tonal noise generated by laminar flow around an airfoil. *J. Acoust. Soc. Am.* **131** (6), EL461–EL467.

DEL ÁLAMO, J.C & JIMÉNEZ, J. 2009 Estimation of turbulent convection velocities and corrections to Taylor's approximation. *J. Fluid Mech.* **640**, 5–26.

DESQUESNES, G, TERRACOL, M & SAGAUT, P 2007 Numerical investigation of the tone noise mechanism over laminar airfoils. *J. Fluid Mech.* **591**, 155–182.

DRAZIN, P. & REID, W. 1981 *Hydrodynamic Stability*. Cambridge University Press.

ELYASI, M. & GHAEMI, S. 2019 Experimental investigation of coherent structures of a three-dimensional separated turbulent boundary layer. *J. Fluid Mech.* **859**, 1–32.

FARGE, M. 1992 Wavelet transforms and their applications to turbulence. *Annu. Rev. Fluid Mech.* **24** (1), 395–458.

FINK, M.R 1975 Prediction of airfoil tone frequencies. *J. Aircraft* **12** (2), 118–120.

FJØRTOFT, R. 1950 *Application of integral theorems in deriving criteria of stability for laminar flows and for the baroclinic circular vortex*. Grøndahl & søns boktr., I kommisjon hos Cammermeyers boghandel. pp. 25–26.

GAO, F., MA, W., ZAMBONINI, G., BOUDET, J., OTTAVY, X., LU, L. & SHAO, L.. 2015 Large-eddy simulation of 3-D corner separation in a linear compressor cascade. *Phys. Fluids* **25**, 085105.

GELOT, M.B.R. & KIM, J. 2020 Effect of serrated trailing edges on aerofoil tonal noise. *J. Fluid Mech.* **904**, A30.

GHAEMI, S., RAGNI, D. & SCARANO, F. 2012 PIV-based pressure fluctuations in the turbulent boundary layer. *Exp. Fluids* **53** (6), 1823–1840.

GLEGG, S.A.L & DEVENPORT, W.J. 2001 Proper orthogonal decomposition of turbulent flows for aeroacoustic and hydroacoustic applications. *J. Sound Vib.* **239** (4), 767–784.

GLEGG, S.A.L & DEVENPORT, W.J. 2017 *Aeroacoustics of Low Mach Number Flow: Fundamentals, Analysis and Measurement*. Academic Press Elsevier.

GOLDSTEIN, M.E. 1983 The evolution of Tollmien–Schlichting waves near a leading edge. *J. Fluid Mech.* **127**, 59–81.

GRANDEMANGE, M. 2013 Analysis and control of three-dimensional turbulent wakes: from axisymmetric bodies to road vehicles. PhD thesis, Ecole polytechnique, Palaiseau, France.

HENNING, A., KAEPERNICK, K., EHRENFRIED, K., KOOP, L. & DILLMANN, A. 2008 Investigation of aeroacoustic noise generation by simultaneous particle image velocimetry and microphone measurements. *Exp. Fluids* **45** (6), 1073–1085.

HOLMES, P., LUMLEY, J.L., BERKOOZ, G. & ROWLEY, C.W. 2012 *Turbulence, Coherent Structures, Dynamical Systems and Symmetry*. Cambridge University Press.

HOWE, M.S. 1978 A review of the theory of trailing edge noise. *J. Sound Vib.* **61** (3), 437–465.

HUERRE, P. & MONKEWITZ, P.A. 1985 Absolute and convective instabilities in free shear layers. *J. Fluid Mech.* **159**, 151–168.

JAISWAL, P., MOREAU, S., AVALLONE, F., RAGNI, D. & PRÖBSTING, S. 2020 On the use of two-point velocity correlation in wall-pressure models for turbulent flow past a trailing edge under adverse pressure gradient. *Phys. Fluids* **32** (10), 105105.

KINGAN, M.J & PEARSE, J.R 2009 Laminar boundary layer instability noise produced by an aerofoil. *J. Sound Vib.* **322** (4-5), 808–828.

KRAICHNAN, R.H. 1967 Inertial ranges in two-dimensional turbulence. *Phys. Fluids* **10** (7), 1417–1423.

KURELEK, J.W., KOTSONIS, M. & YARUSEVYCH, S. 2018 Transition in a separation bubble under tonal and broadband acoustic excitation. *J. Fluid Mech.* **853**, 1–36.

KURELEK, J.W., YARUSEVYCH, S. & KOTSONIS, M. 2019 Vortex merging in a laminar separation bubble under natural and forced conditions. *Phys. Rev. Fluids* **4** (6), 063903.

MA, A., GIBEAU, B. & GHAEMI, S. 2020 Time-resolved topology of turbulent boundary layer separation over the trailing edge of an airfoil. *J. Fluid Mech.* **891**, A1.

MAUCHER, U., RIST, U. & WAGNER, S. 1997 *Secondary Instabilities in a Laminar Separation Bubble*, pp. 229–236. Springer.

MCALPINE, A. 1997 Generation of discrete frequency tones by the flow around an aerofoil. PhD thesis, University of Bristol, United Kingdom.

MICHELIS, T. 2017 Boundary layer separation: Diagnostics and control. PhD thesis, Delft University of Technology, Netherlands.

MICHELIS, T., KOTSONIS, M. & YARUSEVYCH, S. 2018*a* Spanwise flow development within a laminar separation bubble under natural and forced transition. *Exp. Therm. Fluid Sci.* **96**, 169–179.

MICHELIS, T., YARUSEVYCH, S. & KOTSONIS, M. 2018*b* On the origin of spanwise vortex deformations in laminar separation bubbles. *J. Fluid Mech.* **841**, 81–108.

MOREAU, S., LAFFAY, P., IDIER, A. & ATALLA, N. 2016 Several noise control of the trailing-edge noise of a Controlled-Diffusion airfoil. *AIAA Paper* 2016-2816.

MOREAU, S. & ROGER, M. 2005 Effect of airfoil aerodynamic loading on trailing edge noise sources. *AIAA J.* **43** (1), 41–52.

MOREAU, S. & ROGER, M. 2009 Back-scattering correction and further extensions of Amiet's trailing-edge noise model. Part II: application. *J. Sound Vib.* **323** (1-2), 397–425.

MRC STATISTICS 2016 UAV drones–global market outlook (2016–2022). Report ID: SMRC16075.

NAKANO, T, FUJISAWA, N & LEE, S 2006 Measurement of tonal-noise characteristics and periodic flow structure around NACA0018 airfoil. *Exp. Fluids* **40** (3), 482–490.

NASH, E.C., LOWSON, M.V. & MCALPINE, A. 1999 Boundary-layer instability noise on aerofoils. *J. Fluid Mech.* **382**, 27–61.

NOVARA, M. 2013 Advances in tomographic PIV. PhD thesis, Delft University of Technology, Netherlands.

PADOIS, T., LAFFAY, P., IDIER, A. & MOREAU, S. 2015 Detailed experimental investigation of the aeroacoustic field around a Controlled-Diffusion airfoil. *AIAA Paper* 2015-2205.

PADOIS, T., LAFFAY, P., IDIER, A. & MOREAU, S. 2016 Tonal noise of a controlled-diffusion airfoil at low angle of attack and Reynolds number. *J. Acoust. Soc. Am.* **140** (1), EL113–EL118.

DE PANDO, M.F. 2012 Tonal noise generation in flows around aerofoils: a global stability analysis. PhD thesis, Ecole Polytechnique, Palaiseau, France.

DE PANDO, M.F., SCHMID, P.J. & SIPP, D. 2014 A global analysis of tonal noise in flows around aerofoils. *J. Fluid Mech.* **754**, 5–38.

PATERSON, R.W., VOGT, P.G., FINK, M.R. & MUNCH, C.L. 1973 Vortex noise of isolated airfoils. *J. Aircraft* **10** (5), 296–302.

PERENNES, S. & ROGER, M. 1998 Aerodynamic noise of a two-dimensional wing with high-lift devices. *AIAA Paper* 1998-2338.

PRÖBSTING, S. 2015 Airfoil self-noise-investigation with particle image velocimetry. PhD thesis, Technical University of Delft, Netherlands.

PRÖBSTING, S, SCARANO, F & MORRIS, S.C. 2015 Regimes of tonal noise on an airfoil at moderate Reynolds number. *J. Fluid Mech.* **780**, 407–438.

PRÖBSTING, S., SERPIERI, J. & SCARANO, F. 2014 Experimental investigation of aerofoil tonal noise generation. *J. Fluid Mech.* **747**, 656–687.

PRÖBSTING, S & YARUSEVYCH, S 2015 Laminar separation bubble development on an airfoil emitting tonal noise. *J. Fluid Mech.* **780**, 167–191.

PRÖBSTING, S & YARUSEVYCH, S 2021 Airfoil flow receptivity to simulated tonal noise emissions. *Phys. Fluids* **33** (4), 044106.

RAFATI, S & GHAEMI, S 2016 Evaluation of high magnification two and three dimensional particle image tracking/velocimetry in near wall turbulence. In *18th International Symposium on Applications of Laser and Imaging Techniques to Fluid Mechanics, Lisbon, Portugal*.

RAGNI, D., AVALLONE, F., VAN DER VELDEN, W.C.P. & CASALINO, D. 2019 Measurements of near-wall pressure fluctuations for trailing-edge serrations and slits. *Exp. Fluids.* **60** (1), 6.

ROGER, M. & MOREAU, S. 2005 Back-scattering correction and further extensions of Amiet's trailing-edge noise model. Part 1: theory. *J. Sound Vib.* **286** (3), 477–506.

SANJOSE, M., TOWNE, A., JAISWAL, P., MOREAU, S., LELE, S. & MANN, A. 2019 Modal analysis of the laminar boundary layer instability and tonal noise of an airfoil at Reynolds number 150, 000. *Intl J. Aeroacoust.* **18** (2–3), 317–350.

SARIC, W.S., REED, H.L. & KERSCHEN, E.J. 2002 Boundary-layer receptivity to freestream disturbances. *Annu. Rev. Fluid Mech.* **34** (1), 291–319.

SCARANO, F. 2012 Tomographic PIV: principles and practice. *Meas. Sci. Technol.* **24** (1), 012001.

SIROVICH, L. 1987 Turbulence and the dynamics of coherent structures. I. Coherent structures. *Q. Appl. Maths* **45** (3), 561–571.

TAM, C.K.W. 1974 Discrete tones of isolated airfoils. *J. Acoust. Soc. Am.* **55** (6), 1173–1177.

TAM, C.K.W. & JU, H. 2012 Aerofoil tones at moderate Reynolds number. *J. Fluid Mech.* **690**, 536–570.

TAM, C.K.W. & REDDY, N.N. 1977 Sound generated in the vicinity of the trailing edge of an upper surface blown flap. *J. Sound Vib.* **52** (2), 211–232.

THEOFILIS, V., HEIN, S. & DALLMANN, U. 2000 On the origins of unsteadiness and three-dimensionality in a laminar separation bubble. *Phil. Trans. R. Soc. Lond. Ser. A: Math. Phys. Engng Sci.* **358** (1777), 3229–3246.

WANG, M., MOREAU, S., IACCARINO, G. & ROGER, M. 2009 LES prediction of wall-pressure fluctuations and noise of a low-speed airfoil. *Intl J. Aeroacoust.* **8** (3), 177–197.

WATMUFF, J.H. 1999 Evolution of a wave packet into vortex loops in a laminar separation bubble. *J. Fluid Mech.* **397**, 119–169.

WILLMARTH, W.W. & WOOLDRIDGE, C.E. 1962 Measurements of the fluctuating pressure at the wall beneath a thick turbulent boundary layer. *J. Fluid Mech.* **14** (2), 187–210.

WU, H., SANDBERG, R.D. & MOREAU, S. 2021 Stability characteristics of different aerofoil flows at $Re_c = 150\,000$ and the implications for aerofoil self-noise. *J. Sound Vib.* **506**, 116152.

YAKHINA, G. 2017 Experimental study of the tonal trailing-edge noise generated by low-Reynolds number airfoils and comparison with numerical simulations. PhD thesis, Ecole Centrale Lyon, Lyon, France.

YAKHINA, G., ROGER, M., MOREAU, S., NGUYEN, L. & GOLUBEV, V. 2020 Experimental and analytical investigation of the tonal trailing-edge noise radiated by low Reynolds number aerofoils. *Acoustics* **2**, 293–329.

ZAMBONINI, G. & OTTAVY, X. 2015 Unsteady pressure investigations of corner separated flow in a linear compressor cascade. In *ASME Turbo Expo 2015: Turbine Technical Conference and Exposition*, pp. V02CT44A002–V02CT44A002. American Society of Mechanical Engineers.

ZHOU, J., ADRIAN, R.J., BALACHANDAR, S. & KENDALL, T.M. 1999 Mechanisms for generating coherent packets of hairpin vortices in channel flow. *J. Fluid Mech.* **387**, 353–396.